

# The near-infrared spectral index of Sagittarius A\* derived from *Ks*- and *H*-band flare statistics<sup>★</sup>

M. Bremer<sup>1</sup>, G. Witzel<sup>1</sup>, A. Eckart<sup>1,2</sup>, M. Zamaninasab<sup>2,1</sup>, R. M. Buchholz<sup>1</sup>, R. Schödel<sup>3</sup>,  
C. Straubmeier<sup>1</sup>, M. García-Marín<sup>1</sup>, and W. Duschl<sup>4</sup>

<sup>1</sup> I. Physikalisches Institut, Universität zu Köln, Zùlpicher Str.77, 50937 Köln, Germany  
e-mail: [mbremer, witzel, eckart]@ph1.uni-koeln.de

<sup>2</sup> Max-Planck-Institut für Radioastronomie, Auf dem Hügel 69, 53121 Bonn, Germany

<sup>3</sup> Instituto de Astrofísica de Andalucía (CSIC), Glorieta de la Astronomía S/N, 18008 Granada, Spain  
e-mail: rainer@iaa.es

<sup>4</sup> Institut für Theoretische Physik und Astrophysik der Universität zu Kiel, Germany

Received 12 November 2010 / Accepted 7 February 2011

## ABSTRACT

**Context.** The near-infrared (NIR) counterpart of Sagittarius A\* (SgrA\*) at the position of the  $4 \times 10^6 M_{\odot}$  supermassive black hole at the center of the Milky Way has strongly varying flux densities. The broad-band near-infrared spectral index is an essential parameter to determine the underlying emission mechanism for the observed flare emission.

**Aims.** We present a method to derive the NIR spectral index of SgrA\* between the *H*- and *Ks*-band from the statistics of the observed flare emission. Our spectral index derivation is therefore based on an unprecedentedly large timebase of about seven years of monitoring the infrared counterpart of SgrA\*.

**Methods.** We examined NIR light curves of SgrA\* in the *H*- and *Ks*-band and established flare number distributions as a function of peak flare flux. We assume that in both bands the same optically thin dominant emission mechanism is at work and produces similar number distributions of flares. We cross-correlated these histograms and determined a statistical expectation value of the *H-Ks*-band spectral index during the bright phases of SgrA\*.

**Results.** With this new method, we can independently confirm that the expectation value of the spectral index for brighter flares is consistent with  $\alpha = -0.7$  (with the flux density ( $F_{\nu} \propto \nu^{\alpha}$ )) which is expected for pure synchrotron radiation. We find a tendency for weaker flares to exhibit a steeper spectrum.

**Conclusions.** We conclude that the distribution of spectral indices as a function of *Ks*-band flux density can successfully be described by an exponential cutoff proportional to  $\exp[-(\nu/\nu_0)^{0.5}]$  because of synchrotron losses, with  $\nu_0$  being a characteristic cutoff frequency. Varying  $\nu_0$  between the NIR and sub-mm domain and assuming a sub-mm flux density variation of about one Jansky and optically thin spectral indices of  $\alpha = -0.7 \pm 0.3$  explains the observed spectral properties of SgrA\* in the NIR.

**Key words.** black hole physics – infrared: general – accretion, accretion disks – Galaxy: center – Galaxy: nucleus

## 1. Introduction

Stellar dynamics and strongly variable emission allow us to firmly associate Sagittarius A\* (SgrA\*) at the center of the Milky Way with a  $4 \times 10^6 M_{\odot}$  supermassive black hole (SMBH; see Eckart & Genzel 1996; Genzel et al. 1997, 2000; Ghez et al. 1998, 2000, 2003, 2005a, 2008; Eckart et al. 2002; Schödel et al. 2002, 2003, 2009; Eisenhauer et al. 2003, 2005; Gillessen et al. 2009).

Recent observations at wavelengths from the radio to the X-ray domain give detailed insight into the physical emission mechanisms at work in SgrA\*, such as synchrotron, SSC, and bremsstrahlung emission (e.g. Baganoff et al. 2001, 2002, 2003; Eckart et al. 2003, 2004, 2006a,b, 2008a,b, 2009; Porquet et al. 2003, 2008; Goldwurm et al. 2003; Genzel et al. 2003; Ghez et al. 2004b,a; Eisenhauer et al. 2005; Bélanger et al. 2006; Hornstein et al. 2007; Yusef-Zadeh et al. 2006a,b, 2007, 2008, 2009; Marrone et al. 2008; Dodds-Eden et al. 2009; Sabha et al. 2010). The luminosity associated with SgrA\* is of the order of  $10^{-9}$  to  $10^{-10}$  times lower than the Eddington luminosity  $L_{\text{Edd}}$

and many orders of magnitudes below that of SMBHs in active galactic nuclei (AGN) with comparable masses.

In a similar way to results derived for individual flare events, the NIR flare emission has observed spectral indices ( $F_{\nu} \propto \nu^{\alpha}$ ) of  $\alpha \sim -0.6 \pm 0.2$  (Ghez et al. 2005a,b; Hornstein et al. 2007) or even steeper (Eisenhauer et al. 2005; Gillessen et al. 2006). However, the determination of the spectral index is complicated by the correction of the flux contribution of the surrounding blue stars to the emission extracted for SgrA\*. Here we present a new method to calculate the expectation value of the *H/Ks*-band spectral index for the SgrA\* flare emission from the statistics of bright flares in the *H*- and *Ks*-band. This method is based on the comparison of the histograms of flare number versus flare flux. In Sect. 2, we describe the observations and data reduction, and in Sect. 3 present details of the spectral index calculation. Results and conclusions are summarized in Sects. 4 and 5.

## 2. Observations and data reduction

The NIR observations were carried out with the NIR camera CONICA and the adaptive optics (AO) module NAOS (briefly “NACO”) at the ESO VLT unit telescope 4 (YEPUN)

<sup>★</sup> Appendices are available in electronic form at <http://www.aanda.org>

**Table 1.** Statistical information on the NACO *H*-band flares.

Excursion criterion	Total No. of events	Frequency of occurrence [No. of events normalized to 24 h]	Median <i>FWZP</i> [minutes]	Median rising time [minutes]
$4\sigma$	28	19.9	$\geq 14.4$	5.1
$5\sigma$	12	8.5	$\geq 20.0$	14.1

on Paranal, Chile. We restricted our analysis to all *K*s-band ( $2.18 \pm 0.35$ )  $\mu\text{m}$  data taken on observations between 13 June 2003 and 18 May 2009<sup>1</sup> and all *H*-band ( $1.66 \pm 0.33$ )  $\mu\text{m}$  data taken between 29 August 2002 and 22 June 2008. The VLT data sets used in this investigation were all reduced in an identical way to ensure a homogeneous data reduction quality. A detailed analysis of the *K*s-band light curves will be given in a forthcoming paper by Witzel et al. (see also Dodds-Eden et al. 2011). Here we concentrate on the *H*-band data that are essential to understand the short wavelength NIR spectra of SgrA\*. We also include an *H*-band ( $(1.63 \pm 0.30)$   $\mu\text{m}$ ) light curve taken with NIRC at the W. M. Keck telescope on Mauna Kea, Hawaii, USA. Detailed information about the observations and publications used can be taken from Table A.1. Since the *H*-band central filter wavelengths of the different instruments agree with each other to within 10% of their bandwidths, no transformation between them was applied.

A total of 31<sup>2</sup> out of 45 available VLT observation blocks<sup>3</sup> in *H*-band from August 2002 until June 2008 were used for the present analysis. We discarded 14 data sets because of their low quality (strongly variable or insufficient sky transmission, bad seeing, or insufficient AO correction), missing sky or flat exposures, or having observation lengths significantly below 40 min. All *H*-band data cover a total observing time of  $\sim 34$  h. Additional statistical data on the *H*-band observations can be taken from Table 1. The same criteria were used for VLT *K*s-band observations, covering a total of  $\sim 100$  h.

For all observations with the VLT, the infrared wavefront sensor of NAOS was used to lock the AO loop on the NIR bright super-giant IRS 7, located about  $5.6''$  north of SgrA\* (*K*s-band magnitude  $\sim 6.5$ , *H*-band magnitude  $\sim 8.9$  (e.g. Rafelski et al. 2007; Ott et al. 1999; Blum et al. 1996). The images were taken in dither mode. The images of each observation were corrected for sky contributions by subtracting the median of the respective stack of dithered exposures of a dark cloud located about  $400''$  and  $713''$  west of SgrA\*. Furthermore, they were flat-fielded and corrected for dead or bad pixels. These steps were performed with the DPUSER software for astronomical image analysis (T. Ott, MPE; see also Eckart & Duhoux 1990). The PSFs were extracted from these images with *StarFinder* (Diolaiti et al. 2000) and deconvolved with a Lucy-Richardson

<sup>1</sup> For references see Witzel et al. (in prep.).

<sup>2</sup> Based on observations made with ESO Telescope UT4 at Paranal Observatories under program IDs 70.B-0649(B), 71.B-0077(A), 71.B-0077(C), 71.B-0077(D), 71.B-0078(A), 073.B-0084(A), 073.B-0085(A), 073.B-0085(D), 073.B-0775(A), 077.B-0014(A), 077.B-0014(B), 077.B-0014(C), 077.B-0014(E) 077.B-0014(F), 078.B-0136(A), 078.B-0136(B), 179.B-0261(A), 179.B-0261(D), 179.B-0261(T), 273.B-5023(C).

<sup>3</sup> Observations separated by at least 30 min are regarded as independent observation blocks.

(Lucy 1974) algorithm (LR). The beam was subsequently restored with a Gaussian of a *FWHM* near the diffraction limit. These data reduction and deconvolution steps were also taken for polarimetric data (Zamaninasab et al. 2010; Witzel et al. 2011, in prep.). In these cases, flux densities of observations made with the Wollaston prism were obtained by summing the two orthogonal channels. Therefore a total flux for each retarder position can be derived.

The flux densities of the sources were measured by aperture photometry. These apertures were chosen to be small, 2.5 pixels for SgrA\* corresponding to  $67.7$  mas for S27 optics), to minimize any flux contamination by nearby stars. With better seeing, the AO correction improved and the S13 optics was used, enabling us to apply smaller apertures (2.5 pixels corresponding to  $33$  mas) and to minimize any contamination. The calibration and reference stars were measured with an aperture of 4 pixels in both optics. Appropriate corrections were applied to compensate for different aperture sizes (e.g. in the case of background contributions). A correction for extinction was applied, using  $A_K = 2.8$  and  $A_H = 4.3$  for *K*- and *H*-band (Rieke & Lebofsky 1985; Scoville et al. 2003) i.e.  $A_H/A_K = 1.536$ . Within the uncertainties, this is close to the values (i.e.  $A_H/A_{K_s} = 1.598$ ) used by Hornstein et al. (2007), which we later use as a comparison reference for the NIR spectral index of SgrA\*. More recent values of the extinction along the line of sight towards SgrA\* of  $A_{K_s} = 2.54 \pm 0.12$  and  $A_H = 4.48 \pm 0.13$  (i.e.  $A_H/A_{K_s} = 1.764$ ) (Schödel et al. 2010) will result in weaker  $2.2 \mu\text{m}$  intrinsic dereddened flux densities and on average bluer spectral indices.

The flux density calibration was carried out with the known *K*s- and *H*-band flux densities of IRS16C, IRS16NE, and IRS21 by Blum et al. (1996), (see also Schödel et al. 2010). Subsequently precise relative photometry for SgrA\* was performed using up to 14 sources within  $1.5''$  of SgrA\* as secondary calibrators (S67, S27, S26, S96, S6, S7, S8, S35, S51, S83, S86, S30, S100, S98; Gillessen et al. 2010). This results in a flux density of  $\sim 18 \pm 1$  mJy in the *H*-band of the high velocity secondary reference stars S10 and  $\sim 22 \pm 1$  mJy in *K*s-band of S2 (see Ghez et al. 2005b; Eckart et al. 2008b). The measurement uncertainties for SgrA\* were obtained from the standard deviation in the flux density of S10 in *H*-band and S2 in *K*s-band. Images in which the secondary reference stars S10 and S2 deviate by more than  $1.5\sigma$  from their mean were discarded. The background flux in the immediate vicinity of SgrA\* was identified with the average of the measurements at six random locations in a field centered about  $0.6''$  west of SgrA\* that is free of obvious stellar sources. We estimated the systematic error introduced by both the uncertainty in the zero point and extinction to be about  $\sim 10\%$ .

### 3. Calculation of the spectral index

#### 3.1. Flare definition

The flux density variations of Sgr A\* can be explained using either a disk or jet model (see e.g. discussion in Eckart et al. 2006a,b, 2008a), or they could be seen as a consequence of an underlying physical process that can be mathematically described as red-noise with  $\beta = 1$  ( $P(\nu) \propto \nu^{-\beta}$ ), where  $P$  denotes the power spectral density,  $\nu$  is the frequency, and  $\beta$  is the power spectral index (Mauerhan et al. 2005; Eckart et al. 2008a; Do et al. 2009; Zamaninasab et al. 2010). However, Zamaninasab et al. (2010) and Witzel et al. (2011) have demonstrated that highly polarized flare events are statistically significant compared to the randomly polarized red-noise. The

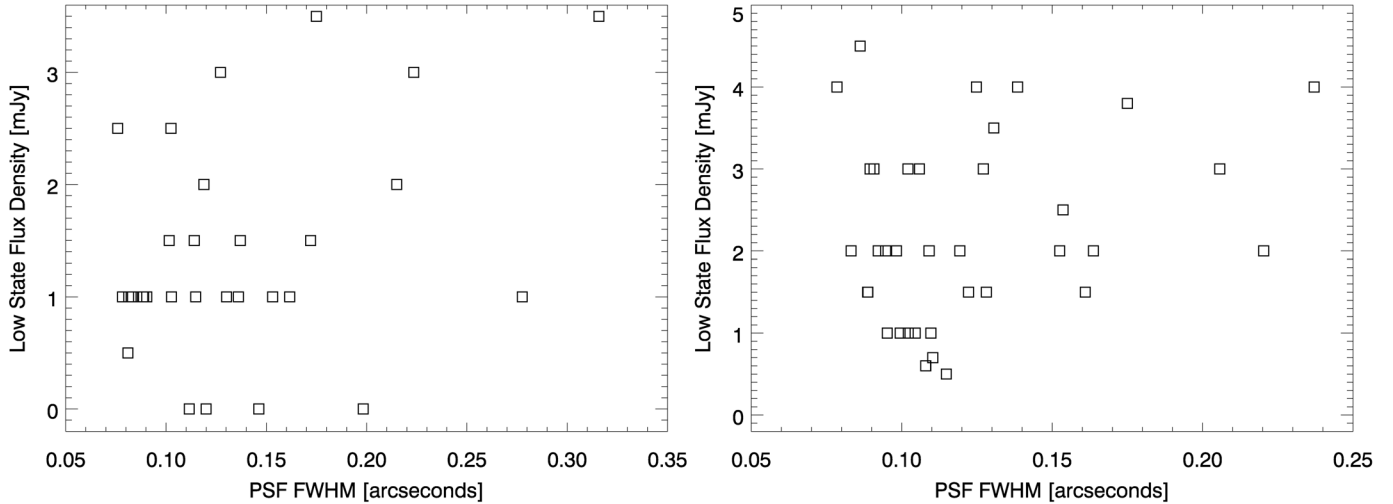


**Fig. 1.** Low state flux density vs. PSF *FWHM* for VLT observations in *H*-band (left panel) and *Ks*-band (right panel).

brightest events in these variations can be considered as flares. In our present analysis, we investigate the distribution of the peak flare flux densities only. This ensures that the influence by any flux density contamination of the stellar background towards SgrA\* is minimized. However, before the properties of these flare events can be examined, one has to establish a definition that assigns an event within the light curve to the group of flares. This definition should include preferably all events, but exclude random statistical fluctuations in the light curve that may be due to the measuring process. A definition based on the rising/decaying flank of an event seems appropriate. To ensure that relatively weak events are counted as flares, a *minimal* deviation of SgrA\*'s light curve of  $4\sigma$  within a time no longer than 15 min was chosen, here  $\sigma$  denotes the standard deviation of the reference star. A second, more restrictive definition was set up to account for clear, strong events only, with flux density excursions of *at least*  $5\sigma$  within a time shorter than 30 min. It is emphasized that almost all of the  $5\sigma$  flares are also covered by the  $4\sigma$  definition. Furthermore, the flux density of a data point, potentially marking the beginning of a flare, has to be higher than or equal to the background flux density. If no rising flank is available, the decaying flank has to meet the selection criteria. A flare is completed when the flux density drops to the initial level at the beginning of the flare or if the end of the observing run terminates the light curve. The  $4\sigma$  criterion is quite sensitive to weak events that occur in phases of low flux density at the position of SgrA\*. In the following, we refer to this phase as the quiescent phase (see also Eckart et al. 2004). These variations are considered as valid events since the quiescent phase can be regarded as a sequence of frequent low-amplitude flares (Eckart et al. 2006b,c). We found 28 (12) events in the *H*-band and 101 (63) in the *Ks*-band fulfilling the  $4\sigma$  ( $5\sigma$ ) criterion. Further statistical data is displayed in Table 1, where the flare frequency corresponds to the number of flares during all *H*-band observations normalized to 24 h. The flare duration is defined by the median *FWZP* measured by the time difference between the data point, at which the light curve leaves the low flux level, and the one, at which it returns to it. If we follow the definition of flare duration by Eckart et al. (2006a), defining periods of increased activity (when the flux density exceeds the average flux plus its standard deviation ( $5.8 \pm 2.2$ ) mJy) with a common duration of 100 min, we derive  $1.6 \pm 0.4$  periods per day.

### 3.2. Measured flux density during the quiescent phase

The origin of the quiescent state mentioned before has not yet been revealed. Eckart et al. (2004) proposed to consider it as a sequence of frequent low amplitude flares but nearby, predominantly blue stars may contribute up to 35% of the flux density at the position of SgrA\* (Sabha et al. 2010). Both mechanisms possibly have to be considered as being relevant. One could expect the flux contamination from nearby stellar sources to depend on the seeing conditions, because with decaying seeing the AO correction becomes less effective and the *FWHM* of the PSF, including its seeing foot, becomes broader. In this case, the flux density contribution from neighboring sources at the position of SgrA\* will increase and small imperfections in the PSF estimate will alienate the flux density of SgrA\* retrieved from the LR-algorithm. Consequently the low flux density phase, if it is dominated by the flux from nearby stars, should correlate with the seeing estimate for the *FWHM* of the PSF. To investigate this effect in more detail, we monitor the width of the PSF of stars close to SgrA\* for each data set through its median *FWHM* value and also estimate the low flux density. Figure 1 show that there is no correlation between the two quantities. A similar result was obtained by Gillessen et al. (2006), who did not find a correlation between the spectral index and the seeing and therefore excluded there being any contamination caused by seeing (i.e. the width of the PSF). This leads to the conclusion that the variable intrinsic flux density contribution of SgrA\* to the flux density measured at its position is also dominant during the low flux density phase. In this case, a constant flux contribution must not be subtracted from the flux density measured during the quiescent phase of SgrA\*. The exact amount of a possible constant contribution of SgrA\* to the quiescent state of a flare is unknown. Dodds-Eden et al. (2011), Sabha et al. (2010), Morris et al. (2007), and Hornstein et al. (2007) stated that SgrA\* may exhibit a quiescent phase with a flux density at or just below 2 mJy in *Ks*-band. The following analysis consequently is performed without any flux density subtraction.

### 3.3. Deriving the spectral index

We now describe the method used to derive the spectral index statistically. The complete methodology is depicted in Fig. 2.

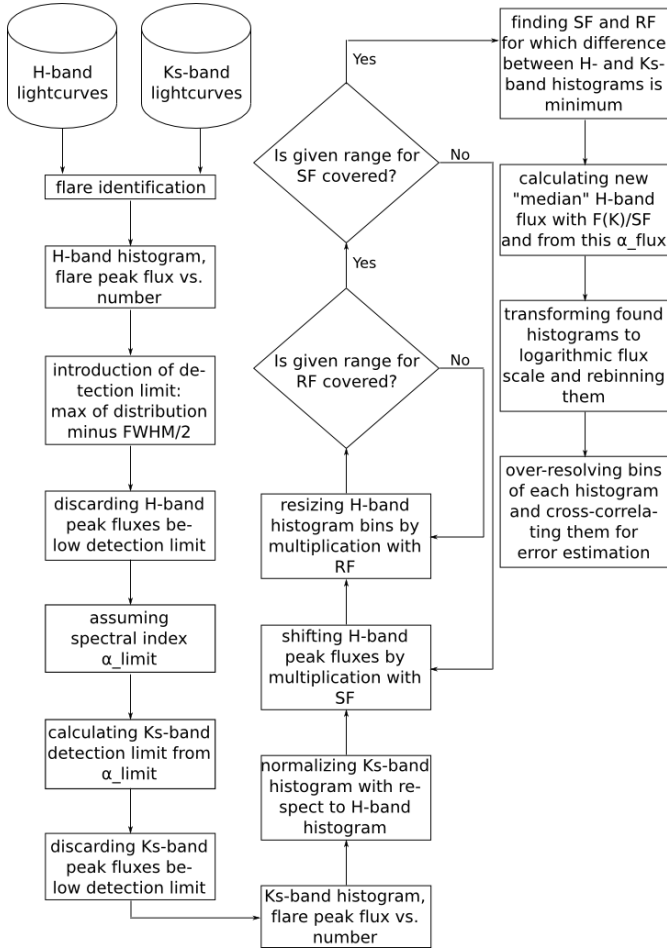


**Fig. 2.** The methodology used in this work to derive the spectral index.

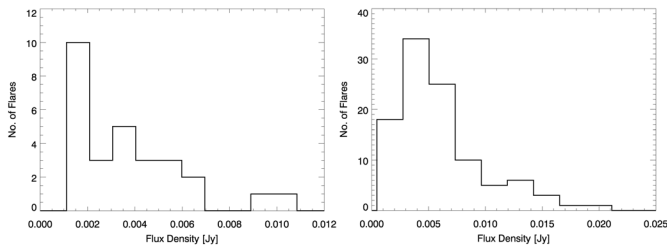


**Fig. 3.** Flux densities and number of occurrence of  $4\sigma$   $H$ -band (left panel) and  $Ks$ -band (right panel) flares.

With the definitions presented in Sect. 3.1, we can construct flux density histograms of SgrA\* in the  $K$ - and  $H$ -band (see Figs. 3 and 4). The median flux density for flares that fulfill the  $4\sigma$  criterion is  $(3.61 \pm 1.62)$  mJy and  $(6.03 \pm 1.85)$  mJy for the  $H$ - and  $Ks$ -band, respectively. Flares fulfilling the  $5\sigma$  criterion have median flux densities of  $(5.94 \pm 0.92)$  mJy in the  $H$ -band and  $(6.72 \pm 1.95)$  mJy in the  $Ks$ -band. The uncertainties are calculated as the median absolute differences from the median flux density value.

We expect the  $H$ - and the  $Ks$ -band flares to be due to the same broad-band emission mechanism that can be described by a power-law distribution. Therefore the shape of the flux density histograms should be identical. Observations indicate that the spectral index is predominantly negative and consequently the  $H$ -band counterparts of weaker  $Ks$ -band flares cannot be detected since they fall below the  $H$ -band detection limit. For this

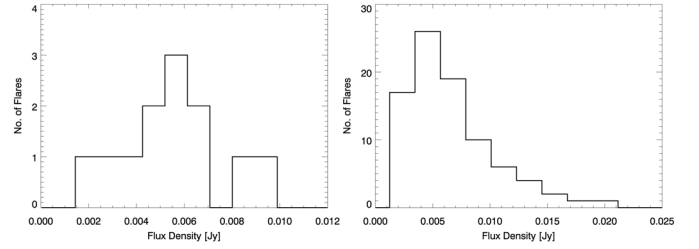


**Fig. 4.** Flux densities and number of occurrence of  $5\sigma$   $H$ -band (left panel) and  $Ks$ -band (right panel) flares.

reason, the  $Ks$ -band flare was matched to the  $H$ -band distribution by systematically reducing the number of  $Ks$ -band flares in the following way. We assume several intrinsic spectral indices  $\alpha_{\text{limit}} = \{0, -0.5, -0.6, -1, -1.5, -2, -2.5, -3, -3.5\}$  ( $F_{\nu} \propto \nu^{+\alpha}$ ). For each value of  $\alpha_{\text{limit}}$ , we create a ten bin histogram with identical bin sizes and then determine the  $H$ -band flare “detection limit” as the lower border of the  $FWHM$  interval of the  $H$ -band flare flux histogram. In combination with  $\alpha_{\text{limit}}$  we then determine the corresponding weakest detectable  $Ks$ -band flux density. All  $Ks$ -band flares below this introduced limit are then discarded. Following this criterion has three advantages:

1. we concentrate on the brighter peak flare fluxes that give a more reliable measurement of the spectral index;
2. we minimize the influence of measurement uncertainties in the peak flux densities of the weakest  $Ks$ -band and corresponding  $H$ -band flares; and
3. we ensure that the spectral index determination is only done using flares that might statistically have been detected in both bands.

To derive an expectation value of the  $H$ - $Ks$ -band NIR spectral index, not only the median values and their median deviations are of interest but also the shapes of the peak flare flux density histograms. To take the shape into account, we normalize the total number of  $Ks$ -band flares to the total number of  $H$ -band flares. We then shift the  $H$ -band flux densities to higher values by multiplying them with a shift factor. The shift factor ( $SF$ ) changes the  $H$ -band flux density by

$$F(H_{\text{new}}) = SF \cdot F(H_{\text{original}}), \quad (1)$$

where  $F(H_{\text{original}})$  denotes the median  $H$ -band flux density of the original distribution and  $F(H_{\text{new}})$  the flux density after shifting  $F(H_{\text{original}})$ . We then determine how well this modified, normalized  $H$ -band distribution matches the shape of the  $Ks$ -band histogram. The  $Ks$ -band histogram is also arranged using ten bins with equidistant bin borders. In the ideal case of perfectly matching  $H$ - and  $Ks$ -band number distributions,  $F(H_{\text{new}})$  will be centered close to the median  $Ks$ -band flux density.

To compare the normalized and scaled histograms independently of binning effects, we allow the  $Ks$ -band bin width to change. As for  $SF$ , a resize factor ( $RF$ ) changes the bin widths of the  $Ks$ -band distribution. If  $B_i$  is the original upper border of bin  $i$ ,  $B_{i,\text{new}}$  is the one after resizing, and  $i = (1 \dots 10)$  is the bin number, then the resize algorithm implies that

$$B_{i,\text{new}} = RF \cdot B_i. \quad (2)$$

In this algorithm, the deviations between the  $H$ - and the  $Ks$ -band distributions are calculated for shift factors  $1 \leq SF \leq SF_{\text{max}}$  in

steps of 0.001, where  $SF_{\max}$  is the maximum shift factor to be taken into account calculated as

$$SF_{\max} = \frac{\text{median}(F(K)) + \text{median}(\Delta F(K))}{\text{median}(F(H_{\text{original}})) - \text{median}(\Delta F(H_{\text{original}}))}, \quad (3)$$

where  $\Delta F$  denotes the deviation of the peak flux density of a flare for the median peak flux from all flares ( $\text{median}(F)$ ). The value for  $RF$  is altered for *each*  $SF$  in steps of 0.001 to a maximum of

$$RF_{\max} = \frac{\text{median}(\Delta(F(K)))}{\text{median}(F(K))}. \quad (4)$$

The standard deviation between the new *H*-band and the *Ks*-band distribution gives a measure of the uncertainty in the match. It is calculated by picking the number of *H*-band flares ( $N_H$ ) and *Ks*-band ( $N_K$ ) flares in bin  $x$  and calculating  $(N_{H_x} - N_{K_x})^2$ . The sum of deviations of all bins in a histogram forms the total deviation. We therefore search for the minimum deviation in the  $SF - RF$ -plane to find the closest match. For example, the standard deviation for the cases where  $\alpha_{\text{limit}}$  equals  $\alpha_{\text{flux}}$  (see Sect. 4, first paragraph) is 6.939 for  $4\sigma$  flares and 0.443 for  $5\sigma$  flares.

The new “median” flux density of the *H*-band distribution is now recovered by dividing the median flux density of the *Ks*-band ( $F(K)$ ) distribution by the  $SF$ . The spectral index is calculated as

$$\alpha_{\text{flux}} = \log\left(\frac{F(H)}{F(K)}\right) / \log\left(\frac{\nu(H)}{\nu(K)}\right). \quad (5)$$

To determine the uncertainty in the relative shift between the two distributions, we assumed that the positive peak flux density values of the flare emission follow a log-normal distribution. We then calculated the logarithms of the fluxes to establish their logarithmic distributions, rebin them, over-resolve each bin by a factor of nine, and perform a cross-correlation between the distributions. To obtain the uncertainty in the relative shift between the two distributions, we fit a Gaussian to the central component of the cross-correlation result (see lower part of Figs. 5 and 6). The standard deviation in this Gaussian then determines the uncertainty and is denoted as  $\Sigma$  (to avoid confusion with the excursion criterion in Sect. 3.1). The uncertainty in  $\alpha$  is now obtained from the spectral indices calculated for both  $F(K) + 10^{\Sigma}$  and  $F(K) - 10^{\Sigma}$ .

## 4. Results

The most reliable result for a spectral index between the *H*- and *Ks*-band is achieved if the *assumed* spectral index, which takes the *H*-band detection limit into account and modifies the lower end of the *H*-band distribution (see previous section), equals the spectral index calculated from the median flux densities, i.e.  $\alpha_{\text{limit}} = \alpha_{\text{flux}}$ . For a lower value of  $\alpha_{\text{limit}}$ , the value of  $\alpha_{\text{flux}}$  will be systematically too small because the lower end of the *K*-band distribution will be over-corrected, resulting in too high a median *K*-band flux density. For a higher value of  $\alpha_{\text{limit}}$ , the value of  $\alpha_{\text{flux}}$  will be severely overestimated because an increasing number of weak flare events will be left in the *K*-band distribution that cannot lead to *H*-band flares above the detection limit. This will lead to too low a median *K*-band flux density.

The closest correspondence is obtained for  $4\sigma$  flares with  $\alpha_{\text{limit}} = -2.5$  and  $\alpha_{\text{flux}} = -2.52 \pm_{0.79}^{1.01}$ . For  $5\sigma$  flares, the uncertainties are even smaller with  $\alpha_{\text{limit}} = -0.5$  and  $\alpha_{\text{flux}} = -0.50 \pm_{0.63}^{0.76}$ .

As an example we show in the upper part of Fig. 5 the logarithmic and re-binned diagram of the closest match of *H*- (black)

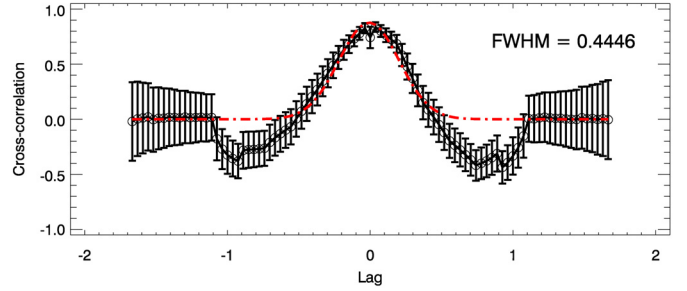
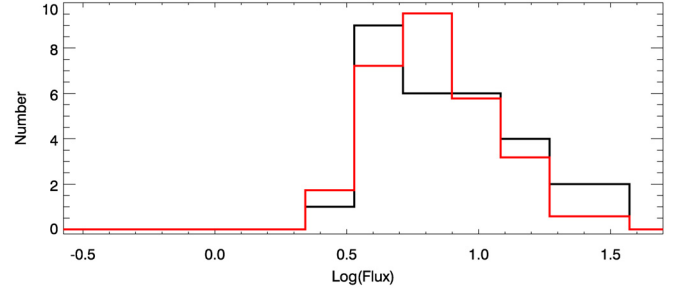


**Fig. 5.** Upper panel: logarithmic and re-binned diagram of the closest match of the *H*- (black) to the *Ks*-band (red) distributions after shifting and resizing the  $4\sigma$  flare distributions (see text for explanation). Lower panel: cross-correlation of both distributions.

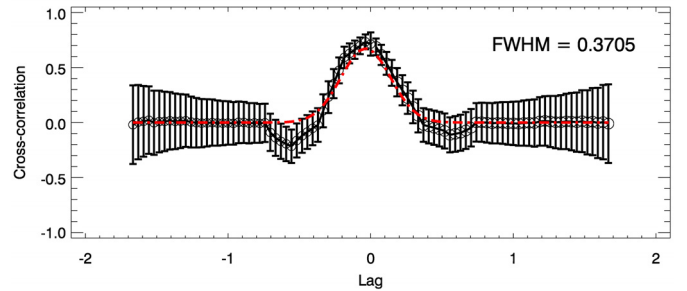
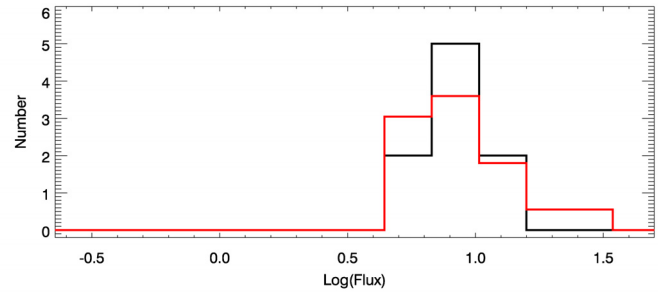


**Fig. 6.** Same as in Fig. 5, but for the  $5\sigma$  flare distributions.

and *Ks*-band (red) distributions after shifting and resizing the  $4\sigma$  flare distributions. The shift factor is 1.989 and the resize factor is 1.250. The number of *Ks*-band flares was reduced by assuming a spectral index of  $\alpha_{\text{limit}} = -2.5$  for the *H*-band flux density, which is equivalent to the distribution maximum minus  $FWHM/2$ , so this *H*-band flux is taken as the flare detection limit. In the lower part of Fig. 5 we present the cross-correlation of the distributions. The logarithmic and re-binned results for the  $5\sigma$  flare distributions are shown in Fig. 6. For these distributions, the derived shift factor is 1.145, and the resize factor is 1.065. A spectral index of  $\alpha_{\text{limit}} = -0.5$  was assumed. The data calculated for all introduced  $\alpha_{\text{limit}}$  is shown in Tables 2 and 3.

**Table 2.** Details on data used and derived for the calculation of the spectral index  $\alpha_{\text{flux}}$  for  $4\sigma$  flares.

$\alpha_{\text{limit}}$	Shift factor $SF$	$FWHM$ of cross- correlation (log(mJy))	Median $F$ ( $K$ ) (mJy)	$F$ ( $H$ ) ( $= \frac{\text{median } F(K)}{SF}$ ) (mJy)	$\alpha_{\text{flux}}$	$\Delta\alpha_{\text{flux}}$
0	1.828	0.4443	6.03	3.30	-2.21	$\pm_{0.84}^{1.09}$
-0.5	1.812	0.4445	6.29	3.47	-2.18	$\pm_{0.81}^{1.03}$
-0.6	1.812	0.4450	6.29	3.47	-2.18	$\pm_{0.81}^{1.03}$
-1.0	1.812	0.4450	6.29	3.47	-2.18	$\pm_{0.81}^{1.03}$
-1.5	1.812	0.4446	6.33	3.49	-2.18	$\pm_{0.80}^{1.03}$
-2.0	1.989	0.4817	6.40	3.22	-2.52	$\pm_{0.82}^{1.06}$
-2.5	1.989	0.4446	6.42	3.23	-2.52	$\pm_{0.79}^{1.01}$
-3.0	1.989	0.4816	6.57	3.30	-2.52	$\pm_{0.80}^{1.03}$
-3.5	2.400	0.4816	6.80	2.83	-3.21	$\pm_{0.78}^{0.99}$

**Notes.** The detection limit for the original  $H$ -band distribution was defined to be the distribution maximum minus  $FWHM/2$ .

**Table 3.** Details of the data used and derived for the calculation of the spectral index  $\alpha_{\text{flux}}$  for  $5\sigma$  flares.

$\alpha_{\text{limit}}$	Shift factor $SF$	$FWHM$ of cross- correlation (log(mJy))	Median $F$ ( $K$ ) (mJy)	$F$ ( $H$ ) ( $= \frac{\text{median } F(K)}{SF}$ ) (mJy)	$\alpha_{\text{flux}}$	$\Delta\alpha_{\text{flux}}$
0	1.145	0.3705	7.41	6.47	-0.50	$\pm_{0.65}^{0.79}$
-0.5	1.145	0.3705	7.71	6.73	-0.50	$\pm_{0.63}^{0.76}$
-0.6	1.174	0.4075	7.81	6.65	-0.59	$\pm_{0.64}^{0.78}$
-1.0	1.306	0.2964	8.23	6.30	-0.98	$\pm_{0.55}^{0.65}$
-1.5	1.289	0.3330	9.20	7.14	-0.93	$\pm_{0.51}^{0.6}$
-2.0	1.437	0.2593	10.00	6.96	-1.33	$\pm_{0.44}^{0.51}$
-2.5	1.658	0.4816	11.98	7.27	-1.86	$\pm_{0.46}^{0.53}$
-3.0	1.997	0.3334	13.34	6.68	-2.54	$\pm_{0.36}^{0.40}$
-3.5	2.166	0.2593	15.12	6.39	-2.84	$\pm_{0.33}^{0.36}$

**Notes.** See Table 2.

The equality of  $\alpha_{\text{limit}}$  and  $\alpha_{\text{flux}}$  is represented in Fig. 7 by the bisecting line (green solid) of the angle defined by the axes. The black (red) solid line is the regression line of the data points for the group of  $4\sigma$  ( $5\sigma$ ) flares. The dotted lines show their respective standard deviation. These deviations depend on the flux density weight of the removed  $Ks$ -band data points relative to the assumed common shape of the  $Ks$ - and  $H$ -band flare flux histograms used to calculate  $\alpha_{\text{flux}}$ . Thus, these deviations are not independent of  $\alpha_{\text{limit}}$  and the uncertainties are underestimated values. We therefore form an uncertainty corridor by the parallel displacement of the regression lines such that they represent the median trend of the positive and negative excursions described by the error bars that stem from the cross-correlation. The intersections of the bisecting line with the regression lines are marked with blue squares and have spectral indices of  $\alpha_{\text{flux},4\sigma} = -2.66_{-0.83}^{+1.03}$  and  $\alpha_{\text{flux},5\sigma} = -0.66_{-0.58}^{+0.63}$ . We drew the median line through both the positive and the negative excursions corresponding to the uncertainties in the cross-correlation, i.e. we illustrated the uncertainties in the uncertainties. Compared to the earlier given values of  $\alpha_{\text{flux}}$ , these are now interpolated values, independent of the discretely sampled  $\alpha_{\text{limit}}$  values. The interpolated values are our more accurate ones.

We derived their corresponding  $Ks$ -band flux densities  $F$  as the weighted average of the  $Ks$ -band fluxes determined from the neighboring  $\alpha_{\text{limit}}$ . The flux uncertainties were calculated the same way. This results in  $F(\alpha_{\text{flux},4\sigma}) = (6.47 \pm 1.56)$  mJy and  $F(\alpha_{\text{flux},5\sigma}) = (7.87 \pm 1.47)$  mJy for the  $4\sigma$  and  $5\sigma$  flares, respectively. The effect of systematic errors (see Sect. 2) on the spectral index is well within the error bars. Data for both flare criteria can be taken from Tables 2 and 3.

The derived values including some of those taken from the literature are compared in Fig. 8. Here the red star with dashed error bars marks the spectral index  $\alpha_{\text{flux},4\sigma} = -2.66_{-0.83}^{+1.03}$  for the amount of flares complying with the  $4\sigma$  criterion. The data point agrees with the values of Krabbe et al. (2006) (blue star) within its uncertainties. The red star with solid error bars marks the spectral index for the set of flares having an excursion steeper than  $5\sigma$ :  $\alpha_{\text{flux},5\sigma} = -0.66_{-0.58}^{+0.63}$ . The value agrees very well with those found by Ghez et al. (2005a). Within its uncertainties, the spectral index  $\alpha_{\text{flux}}$  derived from the  $5\sigma$  flares confirms the previously obtained values of  $\alpha = -0.5 \pm 0.3$  by Ghez et al. (2005a),  $\alpha = -1.2 \pm 0.4$  by Hornstein et al. (2007), as well as the values for bright flares from Gillessen et al. (2006). For clarity the latter two are shown in Fig. 9 rather than Fig. 8.

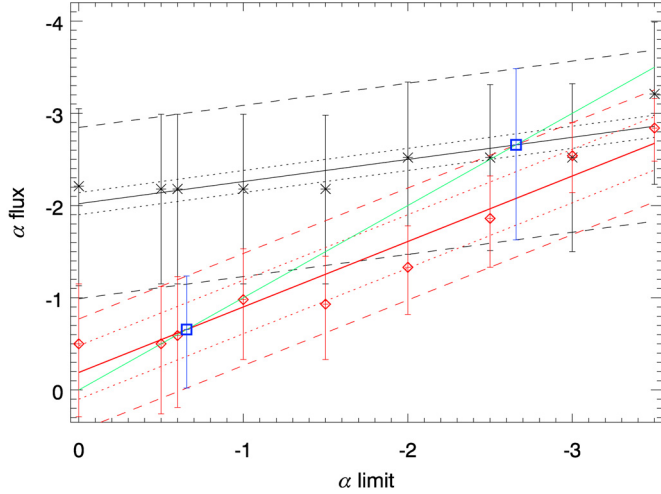


**Fig. 7.**  $\alpha_{\text{limit}}$  vs.  $\alpha_{\text{flux}}$ . Black asterisks (red diamonds): values for  $4\sigma$  ( $5\sigma$ ) flares. Green solid line: bisecting line of the axes' angle. Black (red) solid line: regression line of data points for the set of  $4\sigma$  ( $5\sigma$ ) flares. The dotted lines are their respective standard deviation. The dashed lines form the uncertainty corridor, as described in the text. The blue squares mark the positions of the intersections of the regression lines with the bisecting line.

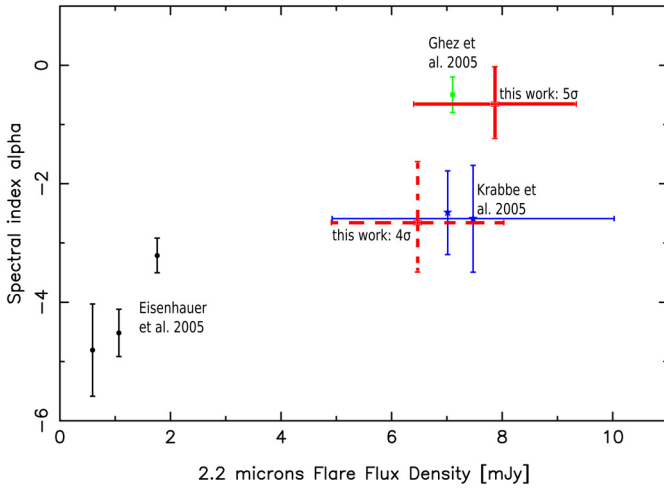


**Fig. 8.** Our derived spectral index values including data taken from the literature (see text).

This supports the assumption that either pure synchrotron radiation or a mixed contribution of synchrotron and synchrotron self-Compton (Eckart et al. 2006a) are the underlying emission mechanisms. Pure synchrotron radiation has an expected spectral index of  $-0.7$  (e.g. Moffet 1975).

The *H-Ks*-spectral index for our set of  $4\sigma$  flares agrees with the value of  $-2.6 \pm 0.9$  found by Krabbe et al. (2006). The spectral index for the  $4\sigma$  flares may also be regarded as being consistent with the flatter of the three otherwise very steep spectral index values of  $\sim -4 \pm 1$  for faint flares reported by Eisenhauer et al. (2005). Hence, our results suggest that the spectral index might depend on the flare flux density, because our  $4\sigma$  flare definition is more dominated by weak flares and variations in the low state flux than the flares obeying the  $5\sigma$  definition.

## 5. Discussion and conclusions

The uncertainty in our spectral index determination for  $5\sigma$  flare events can almost exclude the existence of blue flares (with positive spectral indices) and we consider them as unlikely. Our procedure is not biased *against* blue flares, as blue flares would populate the high flux tail of the *H*-band distribution, which is not modified. In the case of thermal bremsstrahlung, a blue flux density contribution can only occur if a sufficient amount of gas with temperatures  $\ll 10^8$  K is mixed into the central accretion flow or disk. This scenario appears to be unlikely in the case of SgrA\* (see discussions in Yuan et al. 2003; Nayakshin & Sunyaev 2003; Page et al. 2004; Sabha et al. 2010). Blue synchrotron emission must come from the optically thick part of the spectrum (see discussion in Eckart et al. 2009). Synchrotron components with such a high degree of compactness have not yet been reported in the context of SgrA\*.

The *FWHM* values of the *H*- and *Ks*-band flare histograms are similar and the expectation value of the NIR *H-Ks*-band spectral index equals the spectral indices derived from spectroscopic and multicolor data of individual flare events (see references below). Both suggest that the uncertainties in the estimates for individual flares depend more on the statistical variations in the flux densities in the *H*- and *Ks*-bands rather than intrinsic variations in the spectral index. This strongly supports the previous finding that – at least for the bright flares – the NIR emission is produced by pure optically thin synchrotron radiation.

The quiescent level has possibly a different relativistic electron distribution that is responsible for the synchrotron emission, e.g. a variable exponential cutoff in the energy of the electron population may also lead to variable and red spectral indices (Eckart et al. 2006a). The steep spectral indices observed for SgrA\* in the NIR wavelength domain may be due to synchrotron losses, i.e. they may reflect the presence of a cutoff in the relativistic electron distribution (e.g. Eckart et al. 2006a; Liu et al. 2006). This will result in a modulation of the otherwise intrinsically flat spectra with an exponential cutoff proportional to  $\exp[-(\nu/\nu_0)^{0.5}]$  (see e.g. Bregman 1985; and Bogdan & Schlickeiser 1985) and a cutoff frequency of  $\nu_0$  between the infrared and sub-mm wavelength domain. In several extragalactic jets, these cutoffs have also been observed to be relevant for the NIR emission (3C 293: Floyd et al. 2006; M 87: Perlman et al. 2001; Perlman & Wilson 2005; 3C 273: Jester et al. 2001, 2005). In these extragalactic sources the cutoff frequency at which the synchrotron losses become dominant is  $\nu_{\text{jet,break}} = 4 \times 10^{13}$  Hz (corresponding to  $7.5 \mu\text{m}$  wavelength). This is remarkably similar to what may be required in the case of SgrA\*, for which an exponential cutoff in the NIR/MIR wavelength range of  $4\text{--}20 \mu\text{m}$  is suggested by Eckart et al. (2006a). For SgrA\*, this cutoff can quite naturally explain the observed NIR spectral indices reported by several authors (Eisenhauer et al. 2005; Ghez et al. 2005a,b; Hornstein et al. 2007; Gillessen et al. 2006; Krabbe et al. 2006), despite the low upper flux density limits in the MIR (Schödel et al. 2007).

We note that there is a number of flare events that begin before the start or that stop after the end of the light curve. These flares will result in an overestimate of flares with lower peak fluxes. However, we find that the percentage number of these events is, within the uncertainties, the same in the *Ks*- and *H*-band: in the *H*-band 25% of the  $4\sigma$ /50% of the  $5\sigma$  flares and in the *Ks*-band 27% of the  $4\sigma$ /43% of the  $5\sigma$  flares are affected. These flares will therefore alter the peak flare flux histograms in the same way, such that this effect will not have any influence on the result.

**Table 4.** *K*-band spectral indices for pre-flare, dim, and bright states of SgrA\*.

Author	Subtraction method	$\alpha$ Pre-flare	$\alpha$ Dim State	$\alpha$ Bright State
		Flux < 2 mJy	2 mJy $\leq$ Flux $\leq$ 5.5 mJy	Flux > 5.5 mJy
Based on Gillessen et al. (2006)	off state subtr.	$-2.4 \pm 0.8$	$-1.7 \pm 0.8$	$-0.4 \pm 0.4$
	small apertures	$-2.8 \pm 0.6$	$-2.7 \pm 0.8$	$-1.1 \pm 0.6$
	constant subtr.	$-4.4 \pm 0.8$	$-3.3 \pm 0.6$	$-1.3 \pm 0.4$
Based on Hornstein et al. (2007)	off state subtr.	$-2.3 \pm 4.1$	$-1.5 \pm 1.1$	$-1.1 \pm 0.4$
Adopted in this work		$-1.9$ to $-4.3$	$-1.4$ to $-3.1$	$-0.6$ to $-1.6$

**Notes.** Summary of spectral index derivations between NIR bands centered around 1.6  $\mu\text{m}$  and 2.2  $\mu\text{m}$ .

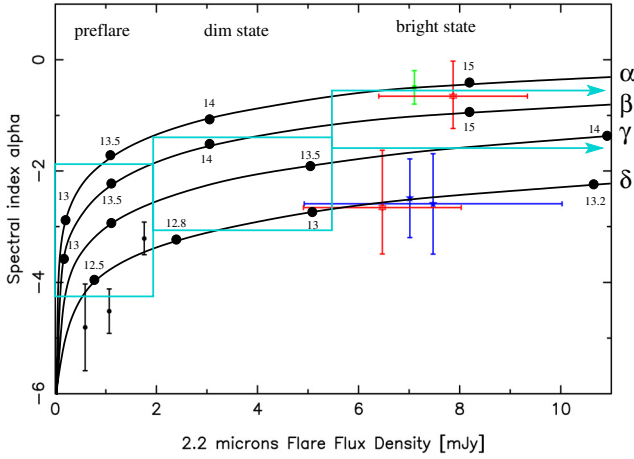


**Fig. 9.** The *H*-*K*<sub>s</sub>-band spectral index versus the de-reddened *K*<sub>s</sub>-band magnitude. The individual data points are described and labeled in Fig. 8. The black dots are the logarithms of the cutoff frequencies and the black solid lines are theoretical curves  $\alpha$  to  $\delta$  explained in the text. These curves are parameterized and labeled with the logarithm of the cutoff frequency. The light blue boxes represent different flux density states using the combined data by Gillessen et al. (2006) and Hornstein et al. (2007) as described in Table 4.

In Fig. 9, we show the relation between the *H*-*K*<sub>s</sub>-band spectral index and the *K*<sub>s</sub>-band flux density calculated for a power law with an exponential cutoff as described above. The thick solid black curves represent different model calculations that cover the expected spectral indices for the synchrotron power law and a flare strength at 1 THz that corresponds well to the degree of variability observed at high frequencies (e.g. Mauerhan et al. 2005). Model  $\alpha$  is based on a power law spectrum with a spectral index of  $\alpha = -0.4$  and a flux density of 0.071 Jy at 1 THz. Curves with higher flux densities would look similar. They would, however, level out to the same value of  $\alpha$  at lower *K*<sub>s</sub>-band fluxes. For model  $\beta$ , the corresponding values are  $\alpha = -0.8$  and 0.5 Jy, for model  $\gamma$  they are  $\alpha = -0.6$  and 0.76 Jy, and for model  $\delta$  they are  $\alpha = -0.4$  and 1.4 Jy. Above 8.5 mJy, model  $\beta$ , and above a *K*<sub>s</sub>-band flux density of 12 mJy, models  $\alpha$ ,  $\gamma$ , and  $\delta$  have 8.6  $\mu\text{m}$  flux densities that are above the 22 mJy flux density limit (Schödel et al. 2007) at which SgrA\* has not yet been detected.

In addition, we show in Fig. 9 light blue rectangular boxes that cover the flux density and NIR spectral index range obtained from the broad-band NIR spectroscopy of Gillessen et al. (2006) (their table in Sect. 4 of the paper) and from the *H*/*K'*-imaging of Hornstein et al. (2007) (their right graph in Fig. 5 of the paper). The values are shown in Table 4.

The data from Hornstein et al. (2007) were treated with a background subtraction method that mostly resembles the

off-state subtraction described by Gillessen et al. (2006), although, the data points were originally not attributed to different activity states. On the basis of Gillessen et al. (2006) three states of activity were defined, which can be attributed to flux densities  $F$  with  $F < 2$  mJy,  $2 \leq F \leq 5.5$  mJy, and  $F > 5.5$  mJy for the pre-flare, the dim state and the bright state, respectively. These values were used by ourselves to dedicate each data point from Hornstein et al. (2007) to an activity state of SgrA\*. From these values, based on both publications including their  $2\sigma$  uncertainty, the median values of their upper and lower limits for each activity state were derived. These median values span areas in the  $\alpha - F$ -plane (rectangular boxes in Fig. 9) that represent the possible combinations of spectral index and flux density for each activity level.

The flux density limit between the pre-flare and the dim state placed at the *K*<sub>s</sub>-band flux density of 2 mJy seems reasonable. This value is currently discussed as the upper limit or actual flux density of a possible low- or quiescent-state of SgrA\* (Do et al. 2009; Sabha et al. 2010; Dodds-Eden et al. 2011). Figure 9 shows that within the model basically all observed spectral indices measured at their corresponding *K*<sub>s</sub>-band flux densities can be explained. For the NIR bright states, all intrinsically weaker flares with flux densities of below about half a Jansky at 1 THz and a cutoff frequency for the synchrotron losses at or above about  $10^{14}$  Hz (3  $\mu\text{m}$  wavelength) are responsible. There is the general tendency that the fainter *K*<sub>s</sub>-band flares with very steep *H*-*K*-band spectra must also be comparatively brighter at cutoff frequencies below  $10^{14}$  Hz. In addition, there is the possibility that a disputed low- or quiescent state may influence the NIR spectral index measurements at the lowest flux densities. An overcorrection of the SgrA\* flux especially in the *H*-band may lead to steeper spectral indices. This is especially a danger for flux densities at or below 2 mJy. The data by Krabbe et al. (2006) who inferred an additional background calibration step actually falls below the measurements of Ghez et al. (2005a,b), Hornstein et al. (2007), and this work.

Finally we also note that the spectral index based on the statistics of the peak values of bright flares equals the spectral indices derived for the bright phases of time-resolved flares (Hornstein et al. 2007; Gillessen et al. 2006). The latter measurements indicate that the spectral index may change on timescales of the individual flare length. These changes could occur if the cutoff frequency  $\nu_0$  at which high frequency synchrotron losses become important varies during a single flare as a function of time. If the flare is correlated with an increase in  $\nu_0$ , one would expect steeper spectra at the beginning and towards the end of the flare. A more detailed investigation of the infrared spectral index of SgrA\*, especially in the low flux density state, requires a higher angular resolution and sensitivity to discriminate the infrared counterpart of SgrA\* from the neighboring stars. This will be possible in the near future using NIR interferometers (VLTI,

the Keck interferometer or interferometry with the LBT) or the planned large aperture telescopes such as the E-ELT.

*Acknowledgements.* Part of this work was supported by COST Action MP0905 Black Hole in a violent Universe. We are grateful to all members of the NAOS/CONICA and the ESO PARANAL team. During this work, M. Zamaninasab was a member of the International Max Planck Research School (IMPRS) for Astronomy and Astrophysics at the MPIfR and the Universities of Bonn and Cologne. R. Schödel acknowledges support by the Ramón y Cajal programme by the Ministerio de Ciencia e Innovación of the government of Spain. Macarena García Marín is supported by the German federal department for education and research (BMBF) under the project numbers 50OS502 and 50OS0801. We thank the referee for helpful and constructive comments.

## References

- Baganoff, F. K., Bautz, M. W., Brandt, W. N., et al. 2001, *Nature*, 413, 45  
 Baganoff, F. K., Bautz, M. W., Ricker, G. R., et al. 2002, in *BAAS*, 34, 1153  
 Baganoff, F. K., Maeda, Y., Morris, M., et al. 2003, *ApJ*, 591, 891  
 Bélanger, G., Terrier, R., de Jager, O. C., Goldwurm, A., & Melia, F. 2006, *J. Phys. Conf. Ser.*, 54, 420  
 Blum, R. D., Sellgren, K., & Depoy, D. L. 1996, *ApJ*, 470, 864  
 Bogdan, T. G., & Schlickeiser, R. 1985, *A&A*, 143, 23  
 Bregman, J. N. 1985, *ApJ*, 288, 32  
 Diolaiti, E., Bendinelli, O., Bonaccini, D., et al. 2000, *A&AS*, 147, 335  
 Do, T., Ghez, A. M., Morris, M. R., et al. 2009, *ApJ*, 691, 1021  
 Dodds-Eden, K., Porquet, D., Trap, G., et al. 2009, *ApJ*, 698, 676  
 Dodds-Eden, K., Gillessen, S., Fritz, T. K., et al. 2011, 728, 37  
 Eckart, A., & Duhoux, P. 1990, *ASPC*, 336, 14  
 Eckart, A., & Genzel, R. 1996, *Nature*, 383, 415  
 Eckart, A., Genzel, R., Ott, T., & Schödel, R. 2002, *MNRAS*, 331, 917  
 Eckart, A., Moultaqa, J., Viehmann, T., et al. 2003, *Astron. Nachr. Suppl.*, 324, 557  
 Eckart, A., Baganoff, F. K., Morris, M., et al. 2004, *A&A*, 427, 1  
 Eckart, A., Baganoff, F. K., Schödel, R., et al. 2006a, *A&A*, 450, 535  
 Eckart, A., Schödel, R., Meyer, L., et al. 2006b, *A&A*, 455, 1  
 Eckart, A., Schödel, R., Meyer, L., et al. 2006c, *J. Phys. Conf. Ser.*, 54, 391  
 Eckart, A., Baganoff, F. K., Zamaninasab, M., et al. 2008a, *A&A*, 479, 625  
 Eckart, A., Schödel, R., García-Marín, M., et al. 2008b, *A&A*, 492, 337  
 Eckart, A., Baganoff, F. K., Morris, M. R., et al. 2009, *A&A*, 500, 935  
 Eisenhauer, F., Schödel, R., Genzel, R., et al. 2003, *ApJ*, 597, L121  
 Eisenhauer, F., Genzel, R., Alexander, T., et al. 2005, *ApJ*, 628, 246  
 Floyd, D. J. E., Perlman, E., Leahy, J. P., et al. 2006, *ApJ*, 639, 23  
 Genzel, R., Eckart, A., Ott, T., & Eisenhauer, F. 1997, *MNRAS*, 291, 219  
 Genzel, R., Pichon, C., Eckart, A., Gerhard, O. E., & Ott, T. 2000, *MNRAS*, 317, 348  
 Genzel, R., Schödel, R., Ott, T., et al. 2003, *Nature*, 425, 934  
 Ghez, A. M., Klein, B. L., Morris, M., & Becklin, E. E. 1998, *ApJ*, 509, 678  
 Ghez, A. M., Morris, M., Becklin, E. E., Tanner, A., & Kremenek, T. 2000, *Nature*, 407, 349  
 Ghez, A. M., Duchêne, G., Matthews, K., et al. 2003, *ApJ*, 586, L127  
 Ghez, A. M., Hornstein, S. D., Bouchez, A., et al. 2004a, in *BAAS*, 36, 1384  
 Ghez, A. M., Wright, S. A., Matthews, K., et al. 2004b, *ApJ*, 601, L159  
 Ghez, A. M., Hornstein, S. D., Lu, J. R., et al. 2005a, *ApJ*, 635, 1087  
 Ghez, A. M., Salim, S., Hornstein, S. D., et al. 2005b, *ApJ*, 620, 744  
 Ghez, A. M., Salim, S., Weinberg, N. N., et al. 2008, *ApJ*, 689, 1044  
 Gillessen, S., Eisenhauer, F., Quataert, E., et al. 2006, *ApJ*, 640, L163  
 Gillessen, S., Eisenhauer, F., Trippe, S., et al. 2009, *ApJ*, 692, 1075  
 Gillessen, S., Eisenhauer, F., Bartko, H., et al. 2010 [arXiv:1002.1224]  
 Goldwurm, A., Brion, E., Goldoni, P., et al. 2003, *ApJ*, 584, 751  
 Hornstein, S. D., Matthews, K., Ghez, A. M., et al. 2007, *ApJ*, 667, 900  
 Jester, S., Röser, H., Meisenheimer, K., Perley, R., & Conway, R. 2001, *A&A*, 373, 447  
 Jester, S., Röser, H., Meisenheimer, K., & Perley, R. 2005, *A&A*, 431, 477  
 Krabbe, A., Iserlohe, C., Larkin, J. E., et al. 2006, *ApJ*, 642, L145  
 Liu, S., Petrosian, V., Melia, F., & Fryer, C. L. 2006, *ApJ*, 648, 1020  
 Lucy, L. B. 1974, *AJ*, 79, 745  
 Marrone, D. P., Baganoff, F. K., Morris, M. R., et al. 2008, *ApJ*, 682, 373  
 Mauerhan, J. C., Morris, M., Walter, F., & Baganoff, F. K. 2005, *ApJ*, 623, L25  
 Moffet, A. T. 1975, *Strong Nonthermal Radio Emission from Galaxies* (the University of Chicago Press), 211  
 Morris, M. R., Hornstein, S. D., Ghez, A. M., et al. 2007, in *IAU Symp.*, ed. V. Karas, & G. Matt, 238, 195  
 Nayakshin, S., & Sunyaev, R. 2003, *MNRAS*, 343, L15  
 Ott, T., Eckart, A., & Genzel, R. 1999, *ApJ*, 523, 248  
 Page, K. L., Reeves, J. N., O'Brien, P. T., Turner, M. J. L., & Worrall, D. M. 2004, *MNRAS*, 353, 133  
 Perlman, E. S., & Wilson, A. S. 2005, *ApJ*, 627, 140  
 Perlman, E. S., Biretta, J. A., Sparks, W. B., Macchetto, F. D., & Leahy, J. P. 2001, *ApJ*, 551, 206  
 Porquet, D., Predehl, P., Aschenbach, B., et al. 2003, *A&A*, 407, L17  
 Porquet, D., Grosso, N., Predehl, P., et al. 2008, *A&A*, 488, 549  
 Rafelski, M., Ghez, A. M., Hornstein, S. D., Lu, J. R., & Morris, M. 2007, *ApJ*, 659, 1241  
 Rieke, G. H., & Lebofsky, M. J. 1985, *ApJ*, 288, 618  
 Sabha, N., Witzel, G., Eckart, A., et al. 2010, *A&A*, 512, A2  
 Schödel, R., Ott, T., Genzel, R., et al. 2002, *Nature*, 419, 694  
 Schödel, R., Ott, T., Genzel, R., et al. 2003, *ApJ*, 596, 1015  
 Schödel, R., Eckart, A., Mužić, K., et al. 2007, *A&A*, 462, L1  
 Schödel, R., Merritt, D., & Eckart, A. 2009, *A&A*, 502, 91  
 Schödel, R., Najarro, F., Muzic, K., & Eckart, A. 2010, *A&A*, 511, A18  
 Scoville, N. Z., Stolovy, S. R., Rieke, M., Christopher, M., & Yusef-Zadeh, F. 2003, *ApJ*, 594, 294  
 Trippe, S., Paumard, T., Ott, T., et al. 2007, *MNRAS*, 375, 764  
 Witzel, G., Eckart, A., Buchholz, R. M., et al. 2011, *A&A*, 525, A130  
 Yuan, F., Quataert, E., & Narayan, R. 2003, *ApJ*, 598, 301  
 Yusef-Zadeh, F., Bushouse, H., Dowell, C. D., et al. 2006a, *ApJ*, 644, 198  
 Yusef-Zadeh, F., Roberts, D., Wardle, M., Heinke, C. O., & Bower, G. C. 2006b, *ApJ*, 650, 189  
 Yusef-Zadeh, F., Wardle, M., Cotton, W. D., Heinke, C. O., & Roberts, D. A. 2007, *ApJ*, 668, L47  
 Yusef-Zadeh, F., Wardle, M., Heinke, C., et al. 2008, *ApJ*, 682, 361  
 Yusef-Zadeh, F., Bushouse, H., Wardle, M., et al. 2009, *ApJ*, 706, 348  
 Zamaninasab, M., Eckart, A., Witzel, G., et al. 2010, *A&A*, 510, A3

Appendix A: Observation in the *H*-band

Table A.1. Details of the analyzed observation runs.

Label	Instrument	Polarized	Used/Discarded	$\lambda$ ( $\mu\text{m}$ )	Pixel scale (mas)	UT		PSF <i>FWHM</i> (mas)	Published in
						Obs. Start Time	Obs. stop time		
1	VLT	–	discarded	1.66	13.22	2002 29 Aug. 23:54:44	2002 30 Aug. 00:48:00	(...)	(...)
2	VLT	–	used	1.66	13.22	2003 19 Mar. 08:33:07	2003 19 Mar. 09:57:17	0.14	here
3	VLT	–	discarded	1.66	13.22	2003 20 Mar. 08:14:07	2003 20 Mar. 08:32:13	(...)	(...)
4	VLT	–	used	1.66	13.22	2003 09 May 06:58:23	2003 09 May 07:58:29	0.08	1,2
5	VLT	–	discarded	1.66	13.22	2003 14 June 04:36:57	2003 14 June 05:04:54	(...)	(...)
6	VLT	–	used	1.66	13.22	2003 14 June 06:01:35	2003 14 June 07:07:49	0.12	here
7	VLT	–	used	1.66	13.22	2003 15 June 05:34:31	2003 15 June 06:59:57	0.09	here
8	VLT	–	used	1.66	13.22	2003 16 June 02:41:59	2003 16 June 04:43:49	0.08	here
9	VLT	–	used	1.66	13.22	2003 21 July 01:08:20	2003 21 July 03:08:37	0.12	here
10	VLT	–	used	1.66	13.22	2003 05 Sep. 00:25:18	2003 05 Sep. 01:08:09	0.08	here
11	VLT	–	used	1.66	13.22	2003 06 Sep. 00:39:03	2003 06 Sep. 01:22:29	0.08	here
12	VLT	–	discarded	1.66	13.22	2004 29 Mar. 06:02:35	2004 29 Mar. 07:41:13	(...)	(...)
13	VLT	–	discarded	1.66	13.22	2004 31 Mar. 06:07:07	2004 31 Mar. 08:02:11	(...)	(...)
14	VLT	–	used	1.66	13.22	2004 29 Apr. 07:29:55	2004 29 Apr. 09:13:53	0.08	here
15	VLT	–	discarded	1.66	13.22	2004 07 May 05:31:19	2004 07 May 05:37:50	(...)	(...)
16	VLT	–	used	1.66	13.22	2004 11 June 05:02:54	2004 11 June 05:41:01	0.08	here
17	VLT	yes	used	1.66	13.22	2004 12 June 04:51:29	2004 12 June 05:54:23	0.08	here
18	VLT	–	used	1.66	13.22	2004 06 July 02:47:58	2004 06 July 03:26:48	0.09	3
19	VLT	–	used	1.66	13.22	2004 08 July 01:53:11	2004 08 July 02:31:04	0.11	here
20	VLT	–	used	1.66	13.22	2004 29 July 04:02:24	2004 29 July 04:50:40	0.22	here
21	VLT	–	discarded	1.66	13.22	2004 24 Sep. 00:17:53	2004 24 Sep. 00:29:51	(...)	(...)
22	VLT	–	used	1.66	13.22	2005 16 May 08:27:15	2005 16 May 10:09:24	0.15	here
23	VLT	–	used	1.66	27.05	2006 29 Apr. 06:55:43	2006 29 Apr. 08:39:25	0.10	here
24	VLT	–	used	1.66	13.22	2006 31 May 03:57:34	2006 31 May 04:58:04	0.14	here
25	VLT	–	used	1.66	13.22	2006 13 June 03:24:08	2006 13 June 05:07:21	0.17	here
26	VLT	–	used	1.66	13.22	2006 29 June 03:56:13	2006 29 June 04:48:21	0.18	here
27	VLT	–	discarded	1.66	13.22	2006 19 July 01:37:18	2006 19 July 01:45:55	(...)	(...)
28	VLT	–	used	1.66	13.22	2006 24 July 00:35:08	2006 24 July 02:45:23	0.22	here
29	VLT	–	used	1.66	13.22	2006 27 July 00:04:45	2006 27 July 01:33:35	0.09	here
30	VLT	–	discarded	1.66	13.22	2006 29 July 00:49:25	2006 29 July 01:42:59	(...)	(...)
31	VLT	–	discarded	1.66	13.22	2006 30 July 23:50:36	2006 30 July 23:51:34	(...)	(...)
32	VLT	–	discarded	1.66	27.05	2006 01 Aug. 23:47:01	2006 02 Aug. 01:00:12	(...)	(...)
33	VLT	–	discarded	1.66	13.22	2006 21 Aug. 23:54:45	2006 22 Aug. 00:13:10	(...)	(...)
34	VLT	–	used	1.66	27.05	2006 28 Aug. 00:26:51	2006 28 Aug. 02:29:13	0.28	here
35	VLT	–	used	1.66	13.22	2006 16 Sep. 00:17:58	2006 16 Sep. 01:15:14	0.32	here
36	VLT	–	used	1.66	13.22	2006 02 Oct. 23:54:51	2006 03 Oct. 00:53:36	0.11	here
37	VLT	–	discarded	1.66	13.22	2006 03 Oct. 00:42:23	2006 03 Oct. 00:45:29	(...)	(...)
38	VLT	–	discarded	1.66	13.22	2006 15 Oct. 00:14:40	2006 15 Oct. 01:01:50	(...)	(...)
39	VLT	–	used	1.66	13.22	2006 15 Oct. 23:38:12	2006 16 Oct. 00:29:57	0.16	here
40	VLT	–	used	1.66	13.22	2007 17 Mar. 07:42:47	2007 17 Mar. 09:08:32	0.10	here
41	VLT	–	used	1.66	13.22	2007 04 Apr. 08:17:35	2007 04 Apr. 09:30:42	0.10	4,5
42	VLT	–	used	1.66	13.22	2007 19 July 04:01:59	2007 19 July 04:37:10	0.12	here
43	VLT	–	used	1.66	13.22	2007 21 July 01:43:27	2007 21 July 02:52:18	0.13	here
44	VLT	–	used	1.66	13.22	2008 21 June 03:42:39	2008 21 June 04:57:20	0.15	here
45	VLT	–	used	1.66	13.22	2008 22 June 06:34:41	2008 22 June 07:09:45	0.20	here
46	Keck	–	used	1.63	20.6	2005 31 July ~ 07:00:00	2005 31 July ~ 09:00:00	(...)	6

**References.** (1) Genzel et al. (2003); (2) Trippe et al. (2007); (3) Eckart et al. (2006a); (4) Yusef-Zadeh et al. (2009); (5) Dodds-Eden et al. (2009); (6) Hornstein et al. (2007).

## Appendix B: *H*-band lightcurves used in this work

In the following, the *H*-band lightcurves used are displayed (see Table A.1). In general in the upper panel of each figure the lower black datapoints mark the background measurements, the upper black curve shows the reference star S10 (if another reference star is used it is explicitly mentioned in the caption), and the green curve represents the flux density development of SgrA\*. The lower panel shows the observational conditions by the *FWHM* of the 2-dimensional PSF (red in the direction of right ascension, purple in the direction of declination).

19 March 2003

08:33:07 to 09:57:17

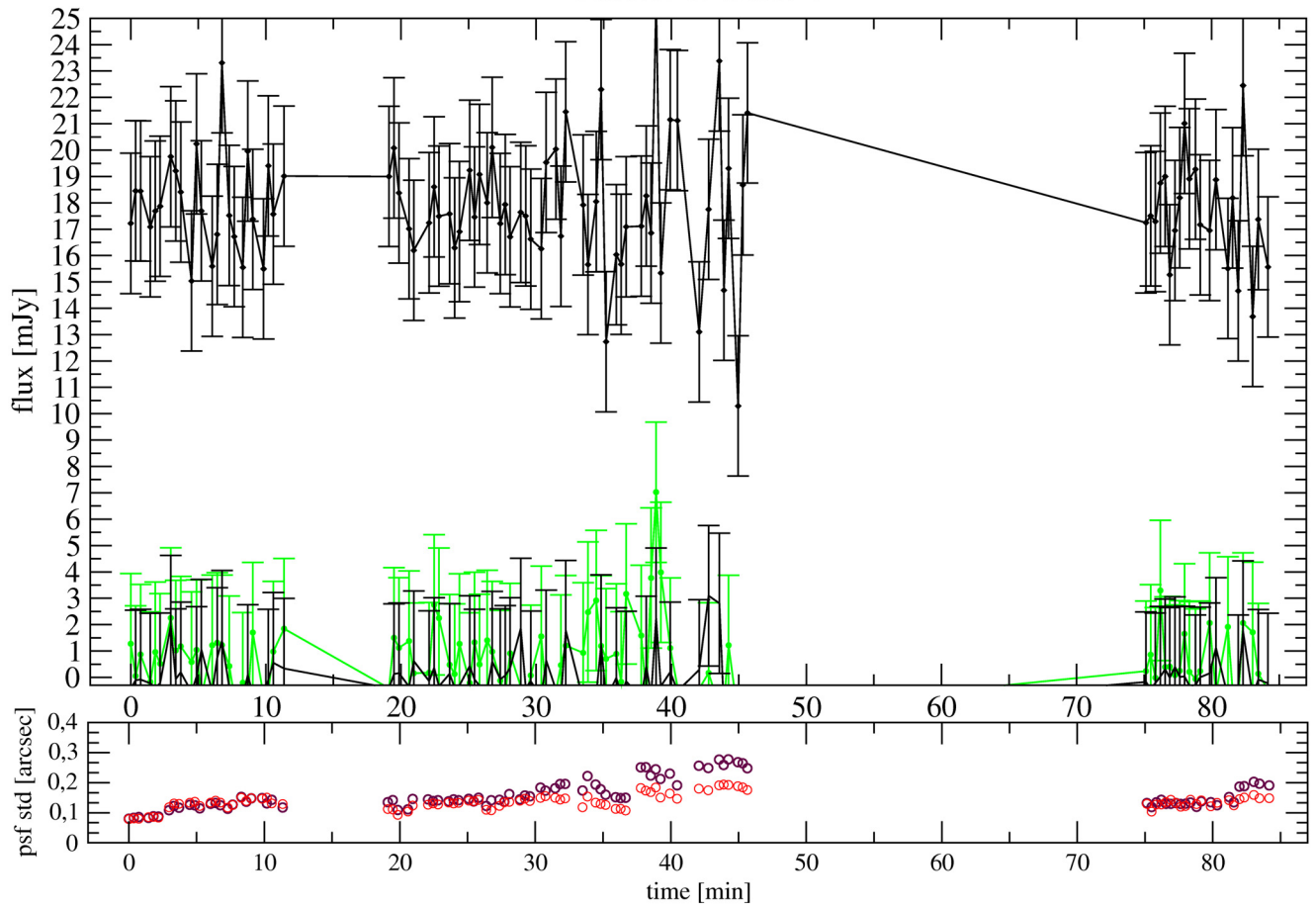


**Fig. B.1.** Observation from 19 March 2003.

9 May 2003

06:58:23 to 07:58:29

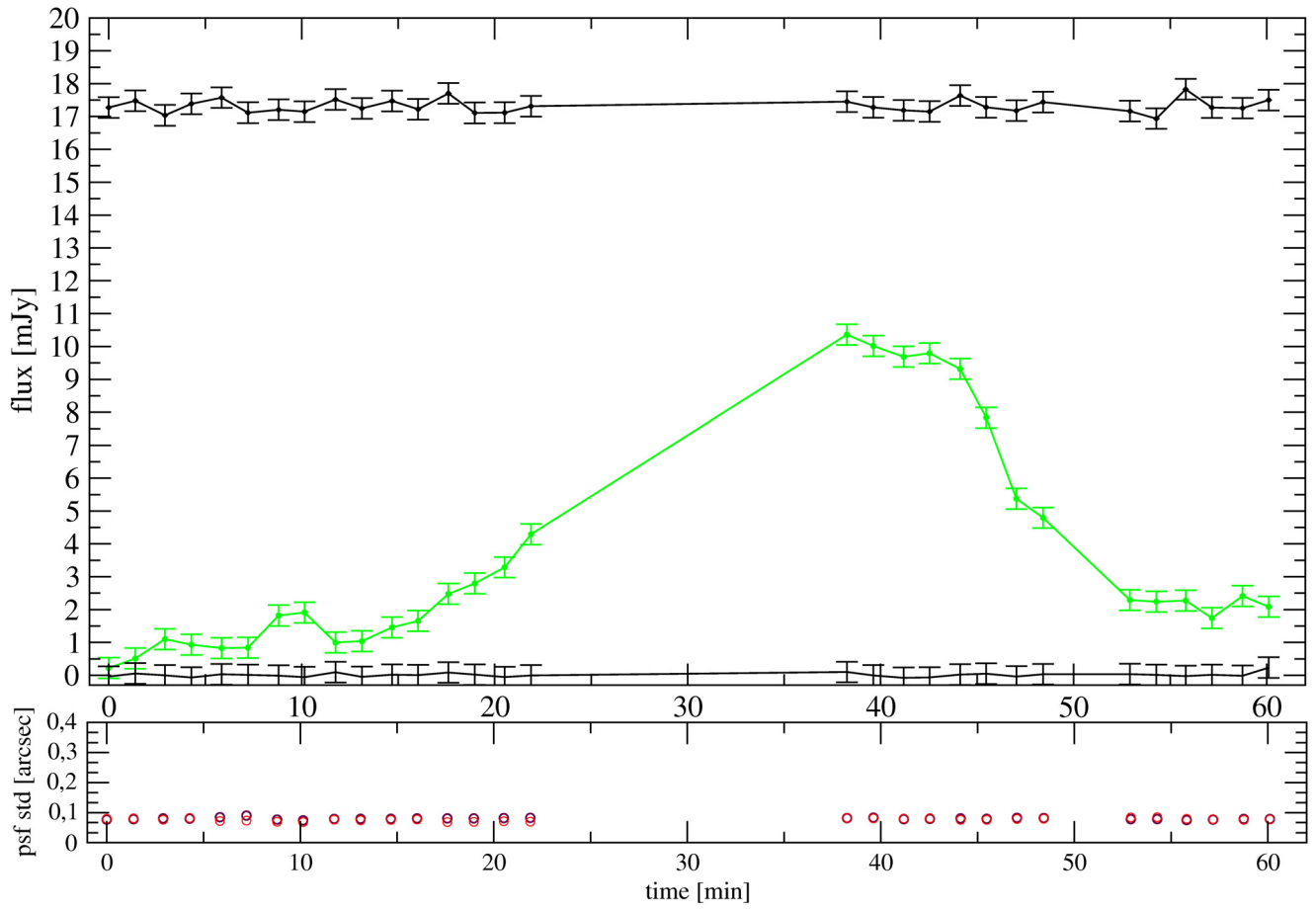


Fig. B.2. Observation from 9 May 2003.

14 June 2003

06:01:35 to 07:07:49

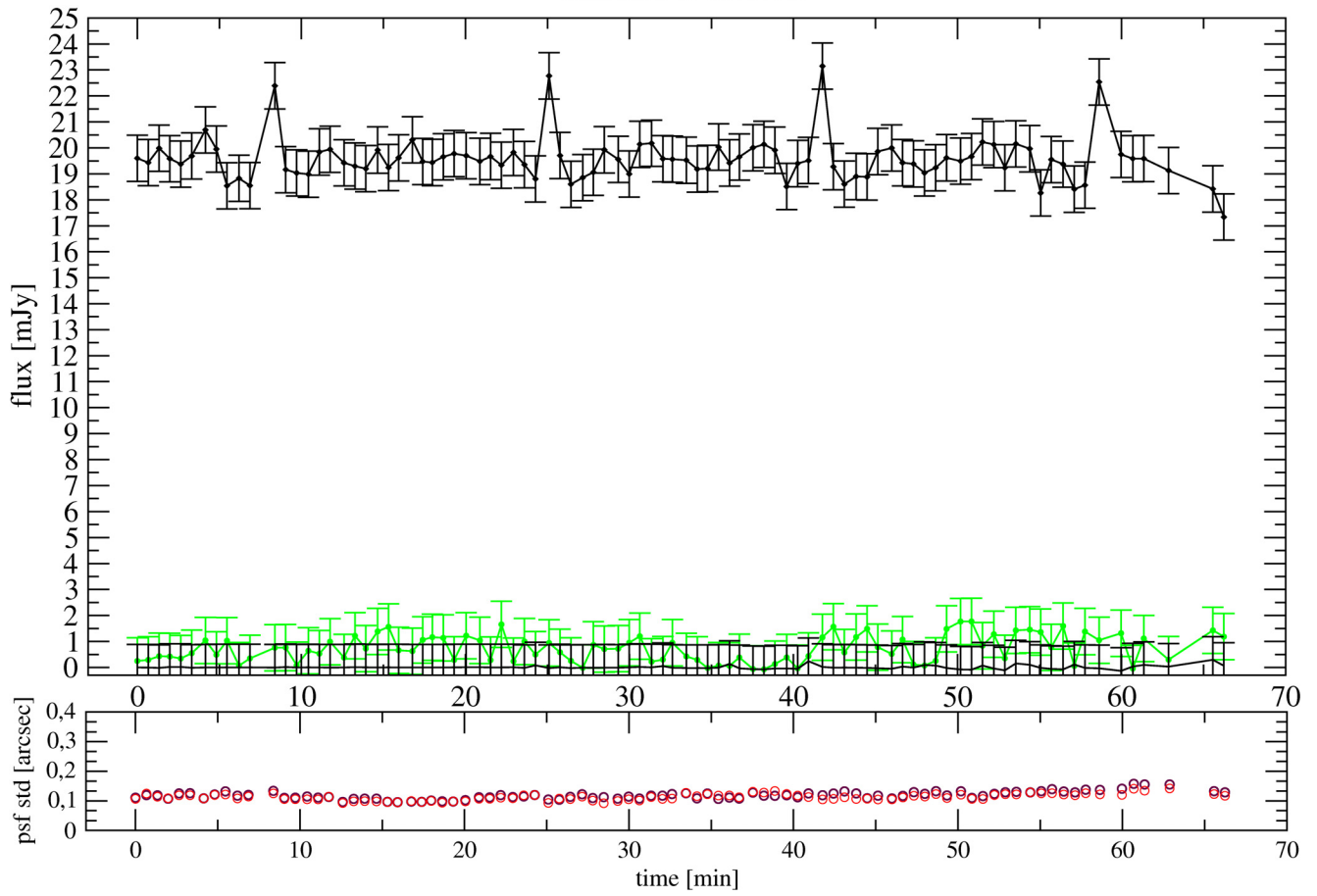
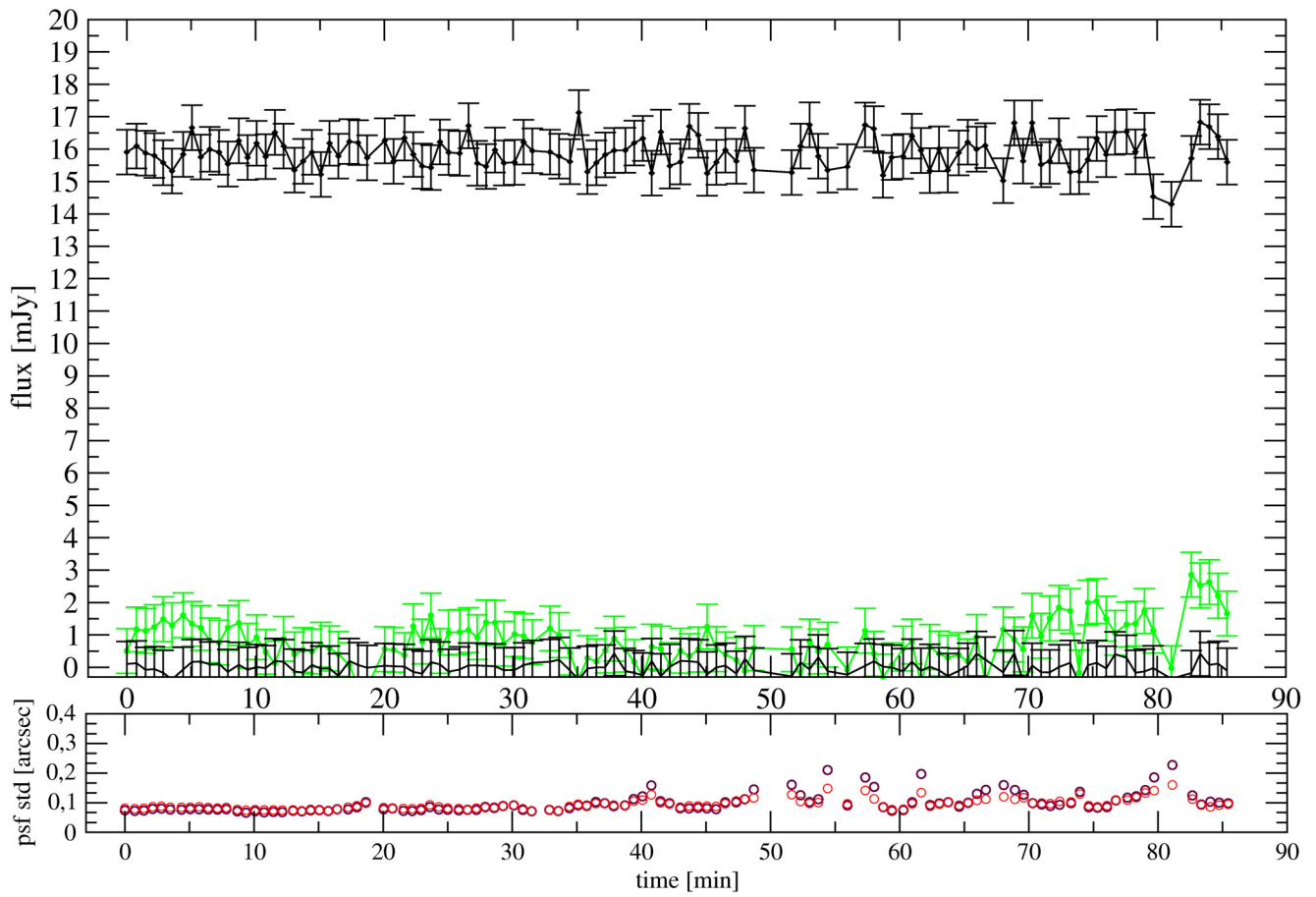


Fig. B.3. Observation from 14 June 2003.

15 June 2003

05:34:31 to 06:59:57



**Fig. B.4.** Observation from 15 June 2003.

16 June 2003

02:41:59 to 04:43:49

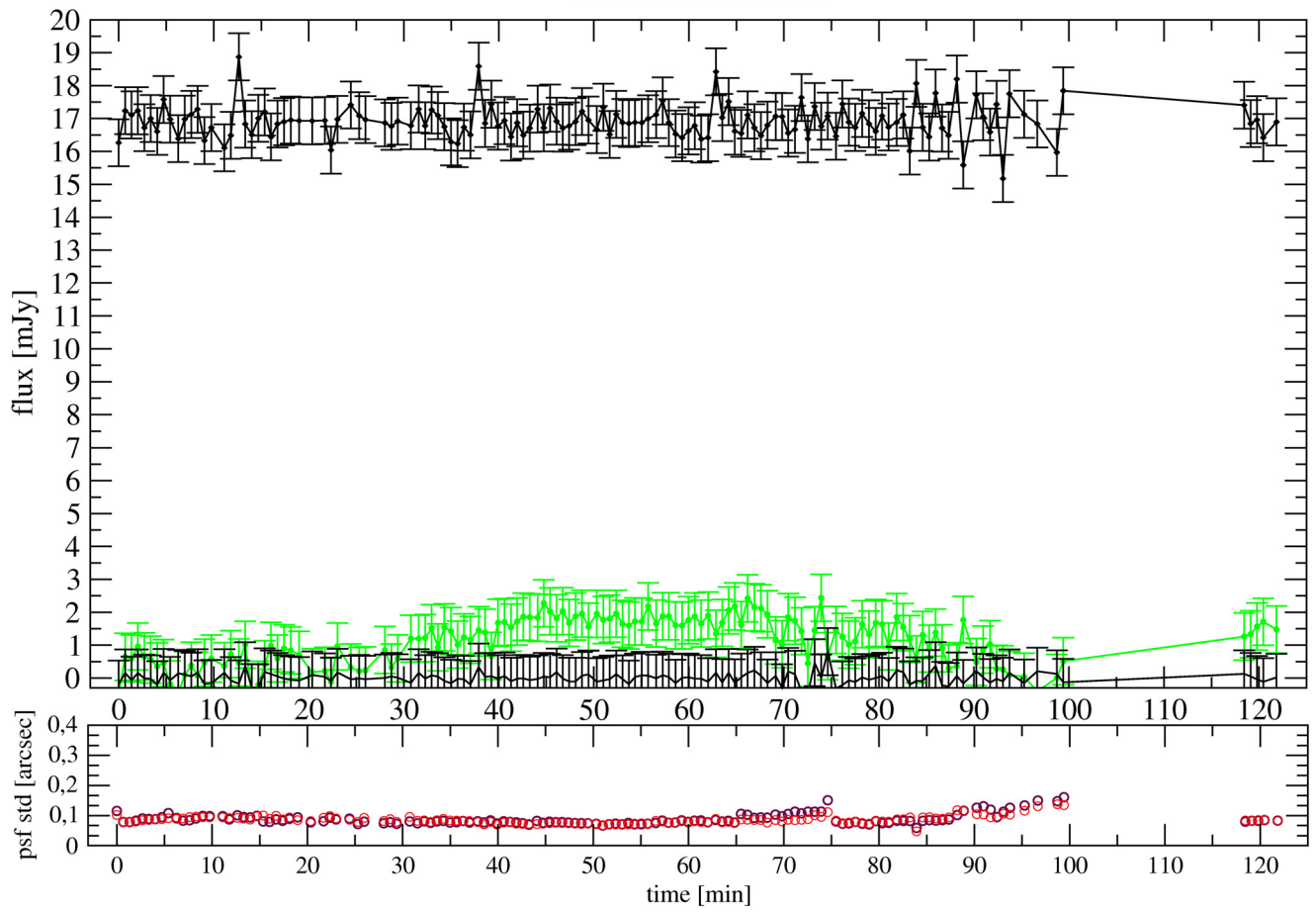


**Fig. B.5.** Observation from 16 June 2003.

21 July 2003

01:11:15 to 02:56:35

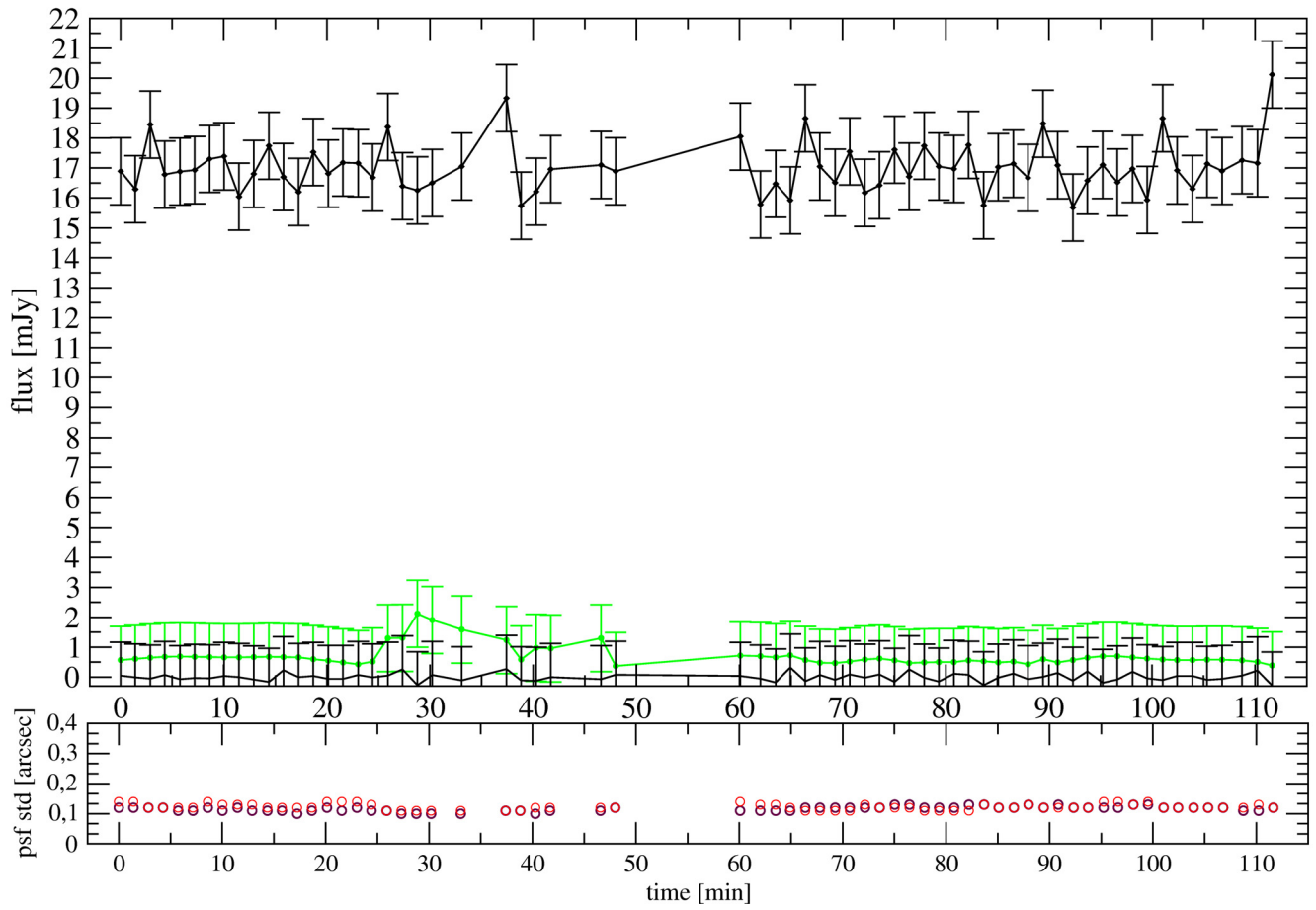


Fig. B.6. Observation from 21 July 2003.

5 September 2003

00:25:18 to 01:08:09

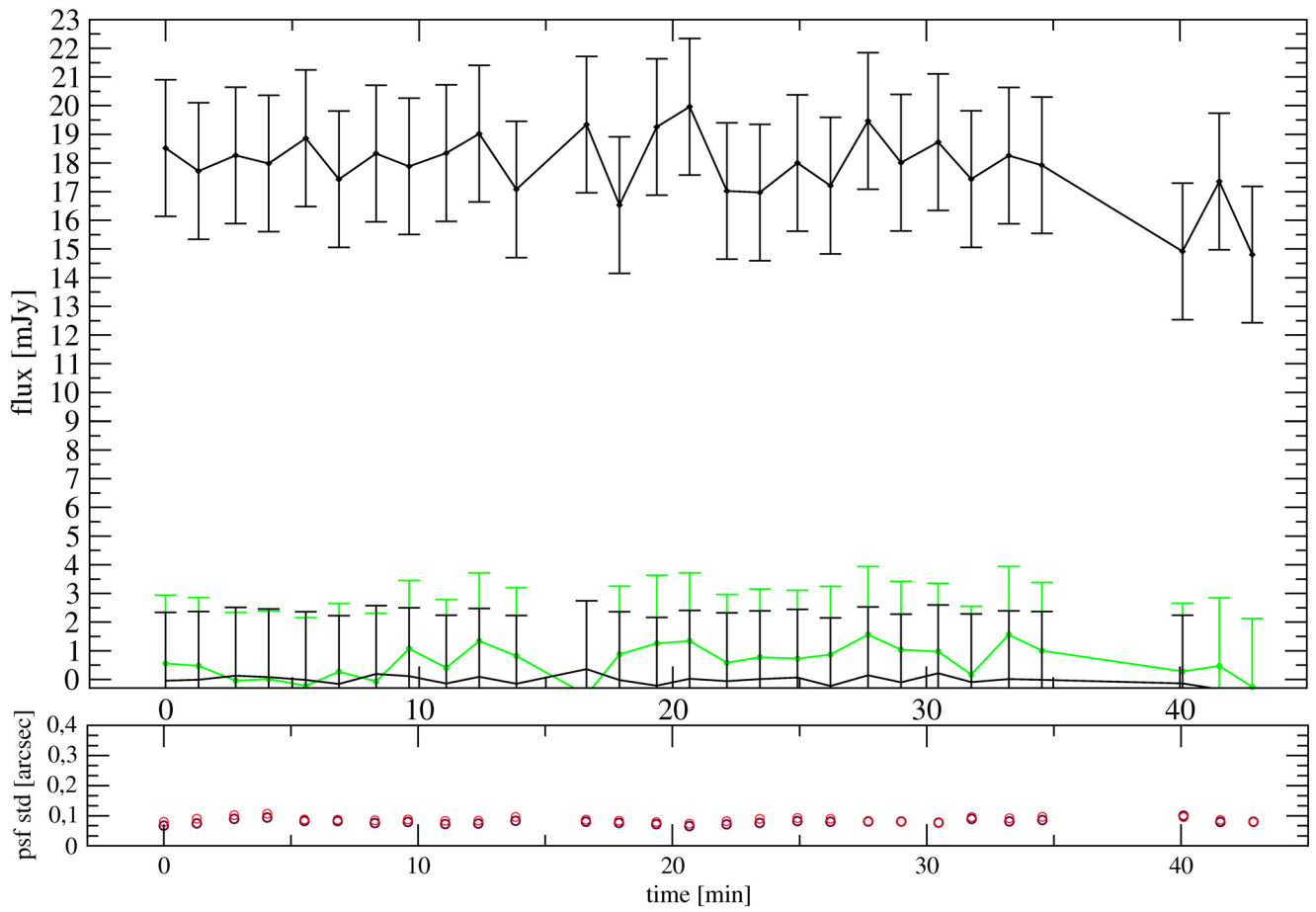


Fig. B.7. Observation from 5 September 2003.

6 September 2003

00:40:23 to 01:22:29

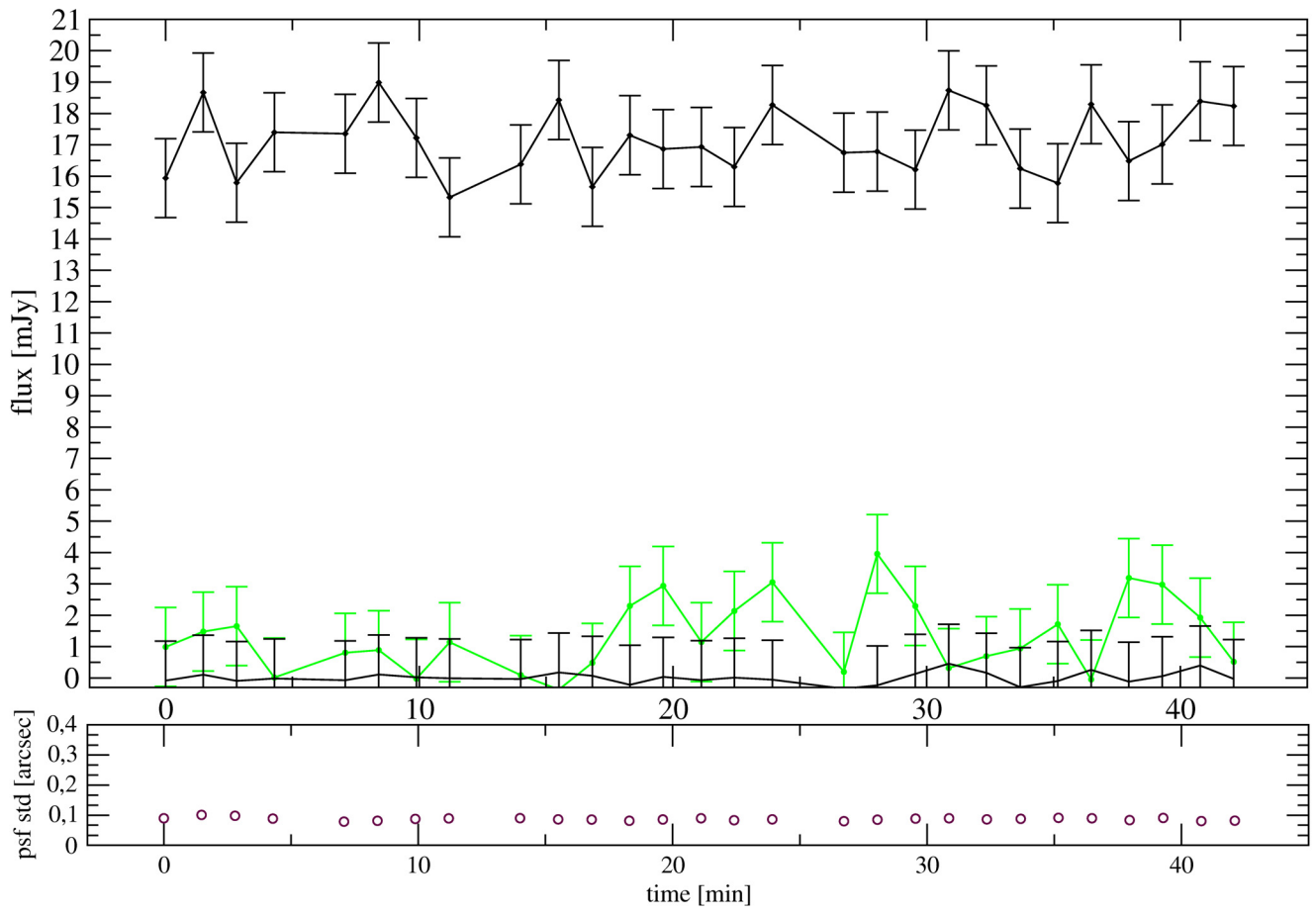


Fig. B.8. Observation from 6 September 2003.

29 April 2004

07:29:55 to 09:13:53

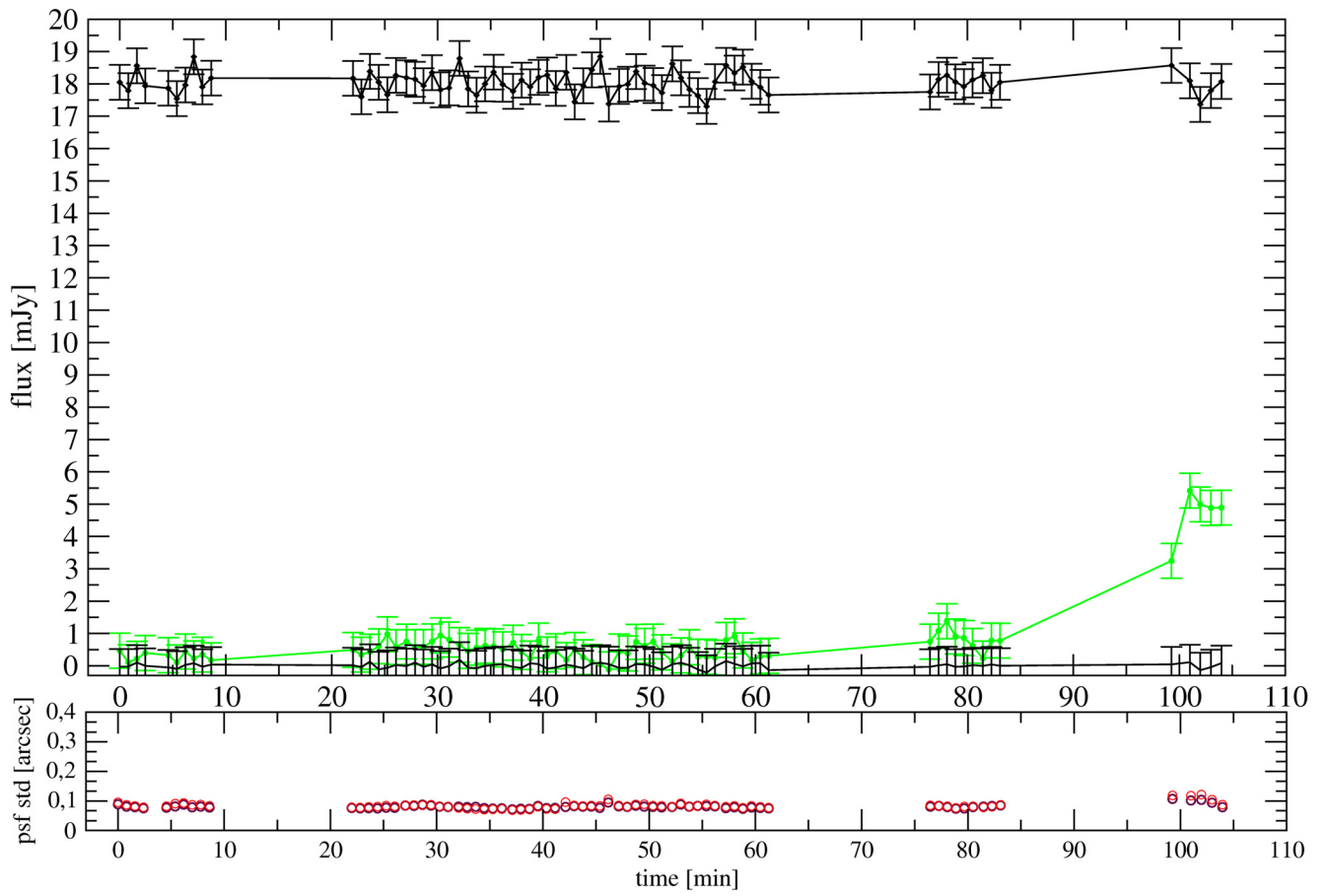
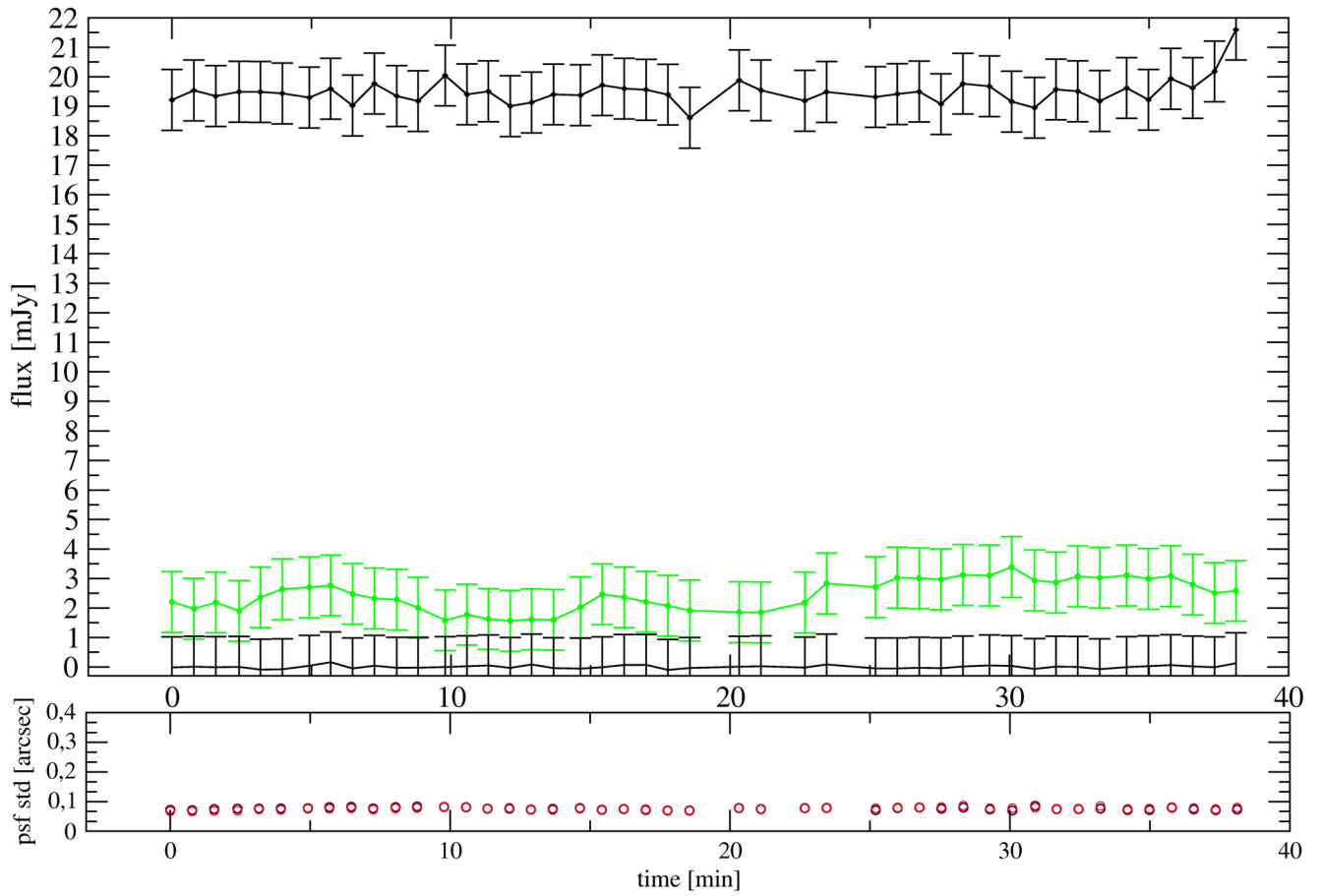


Fig. B.9. Observation from 29 April 2004.

11 June 2004

05:02:54 to 05:41:01



**Fig. B.10.** Observation from 11 June 2004.

12 June 2004

04:52:27 to 05:54:23

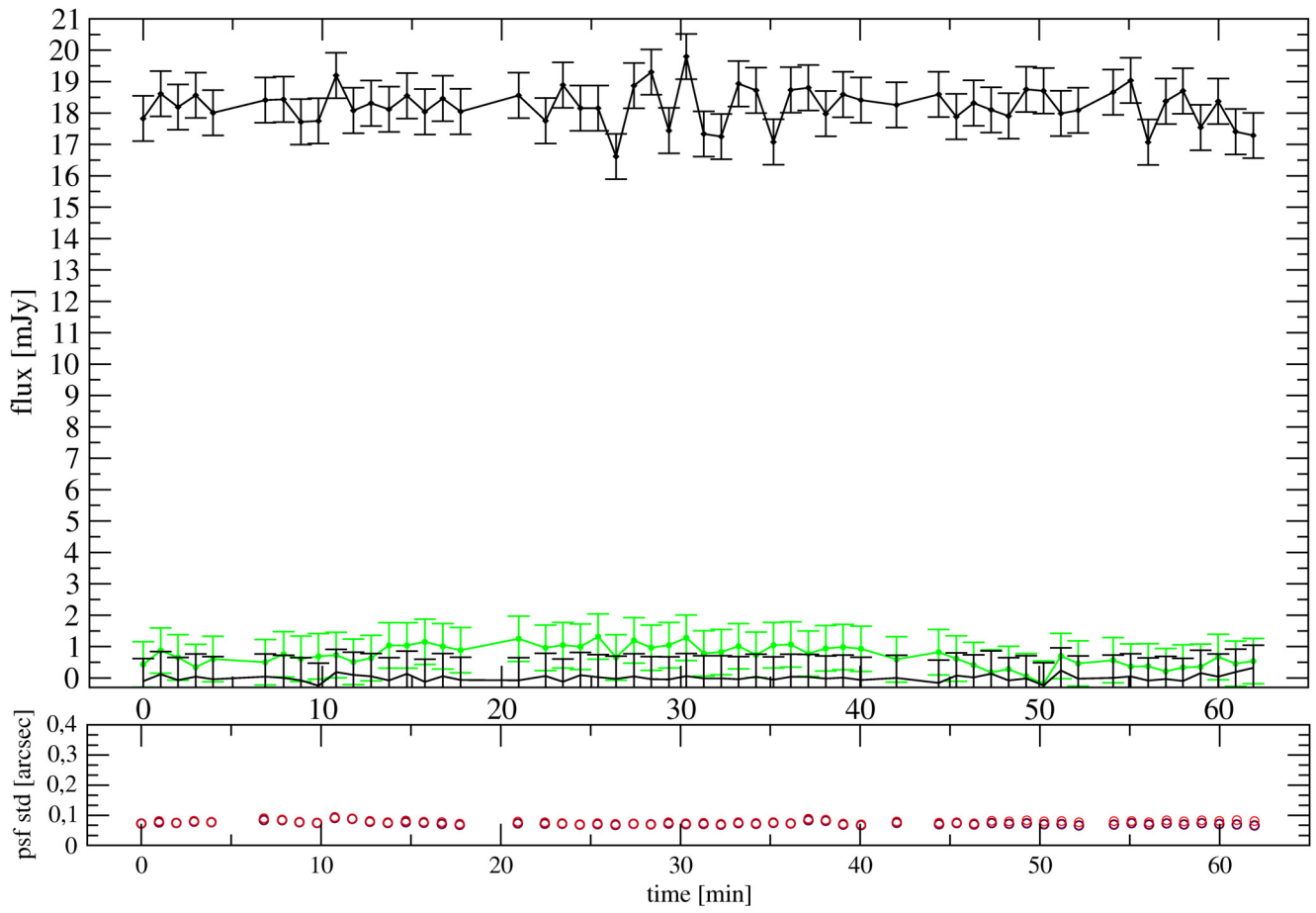


Fig. B.11. Observation from 12 June 2004.

6 July 2004

02:49:26 to 03:26:48

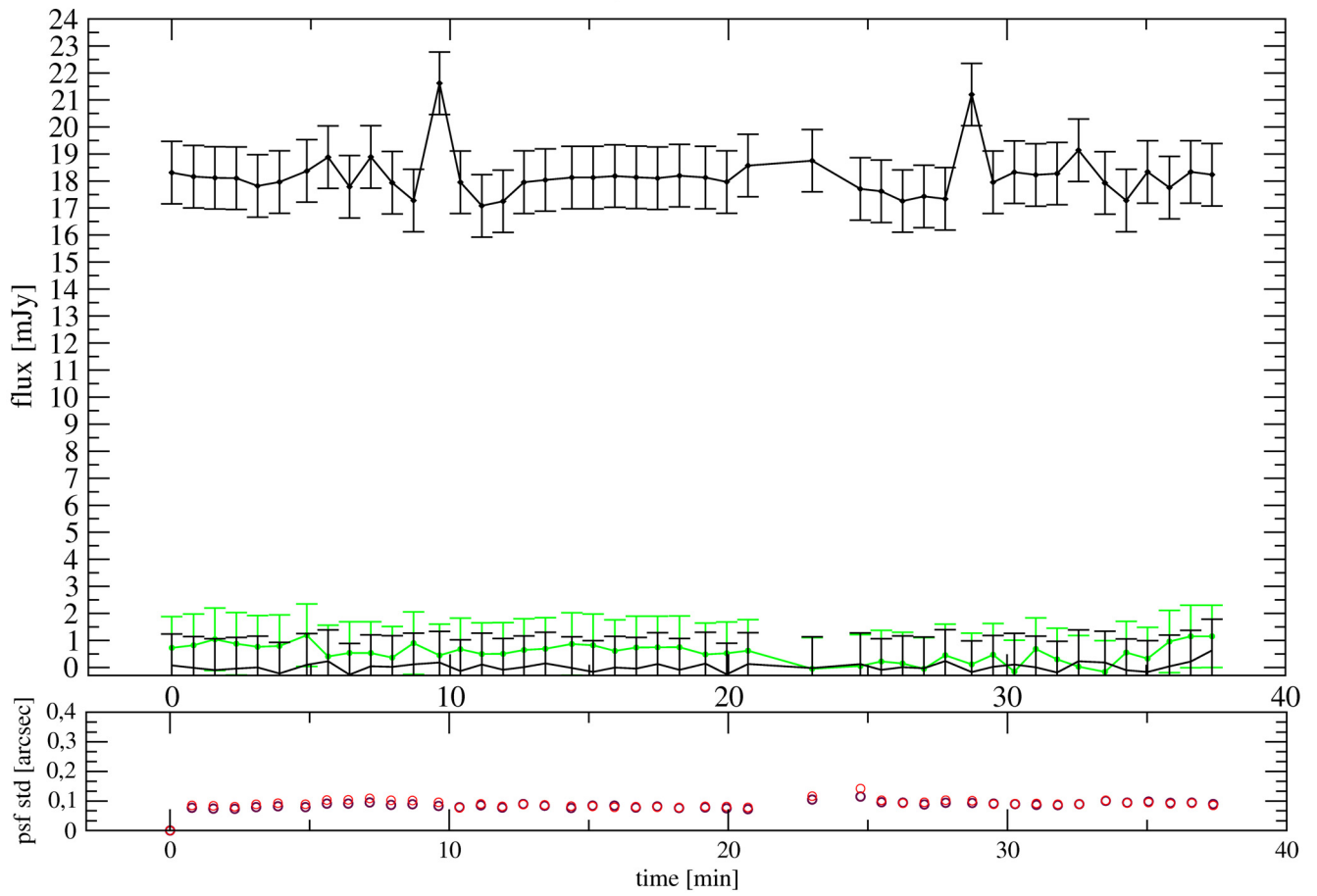


Fig. B.12. Observation from 6 July 2004.

8 July 2004

01:53:58 to 02:31:04

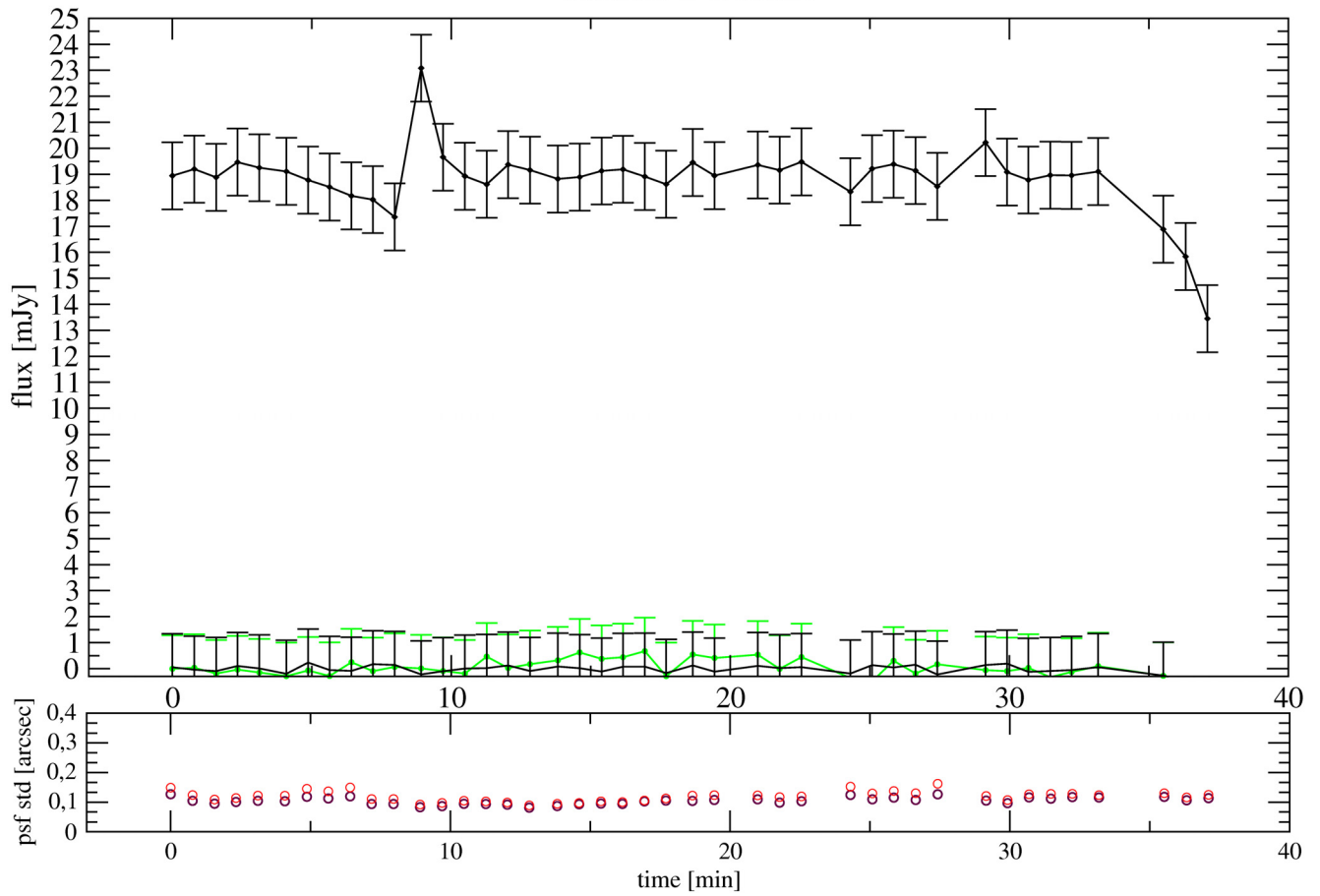
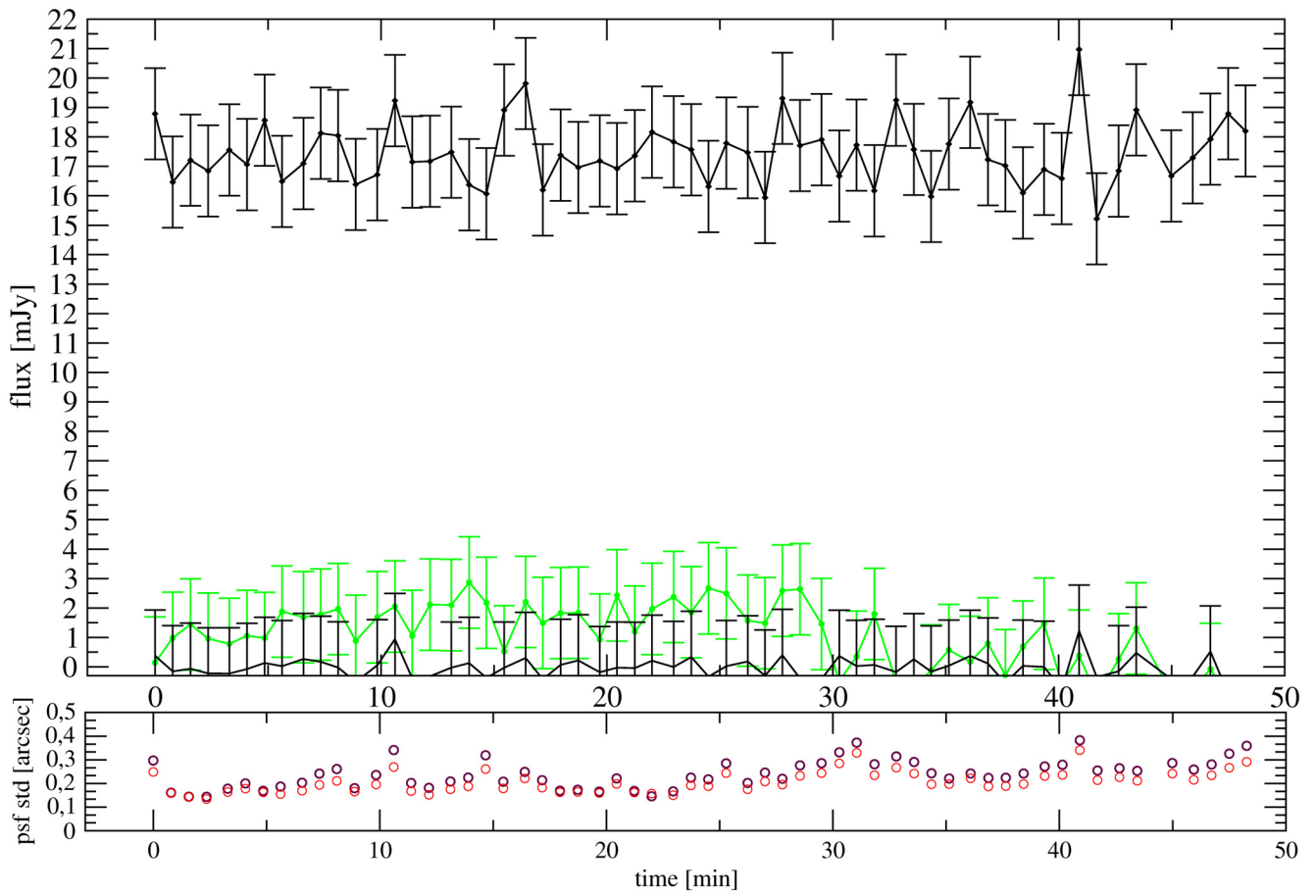


Fig. B.13. Observation from 8 July 2004.

29 July 2004

04:02:24 to 04:50:40



**Fig. B.14.** Observation from 29 July 2004.

16 May 2005

08:27:15 to 10:09:24

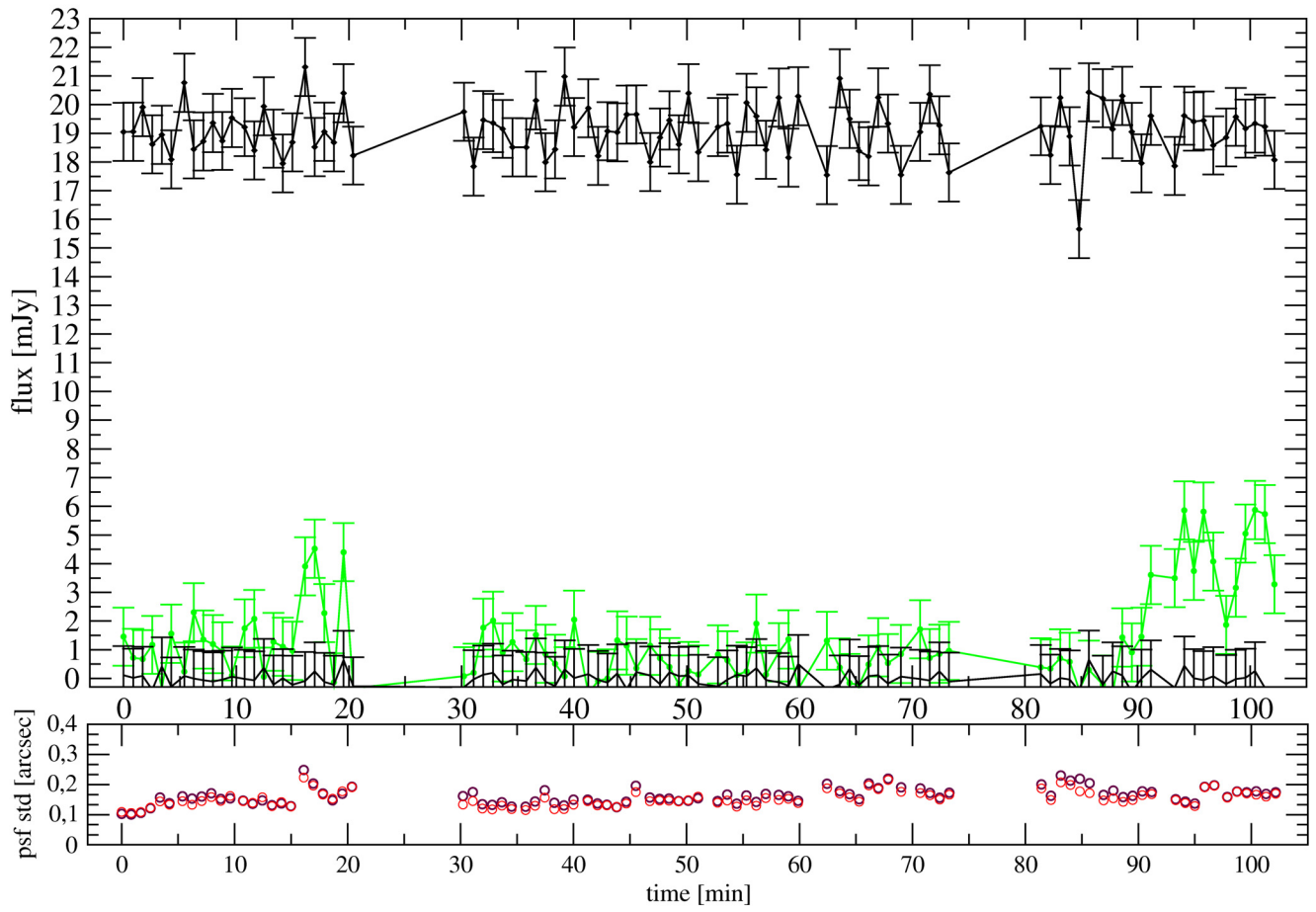


**Fig. B.15.** Observation from 16 May 2005.

29 April 2006

08:02:04 to 08:50:50

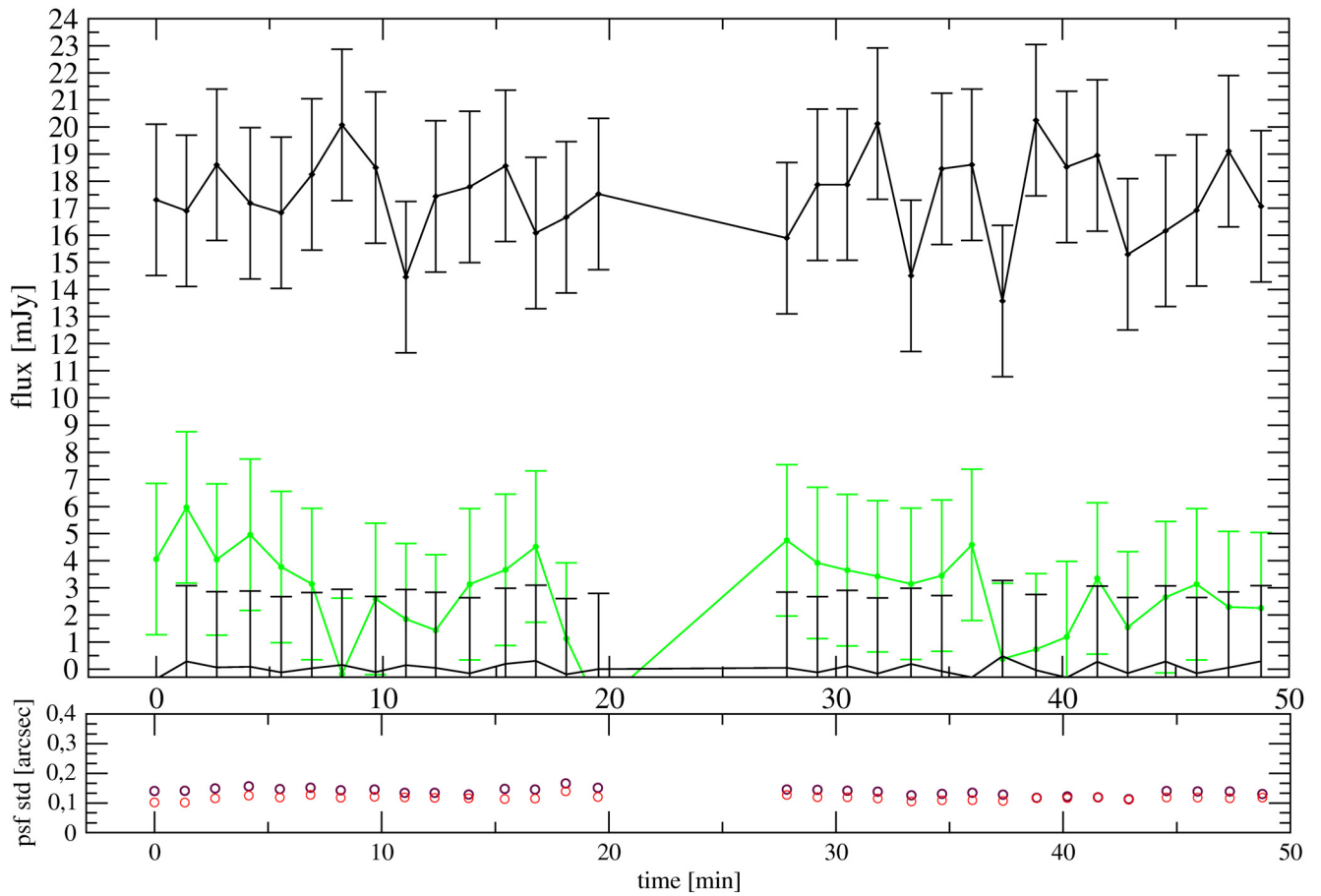


Fig. B.16. Observation from 29 April 2006.

29 April 2006

06:56:41 to 07:53:26

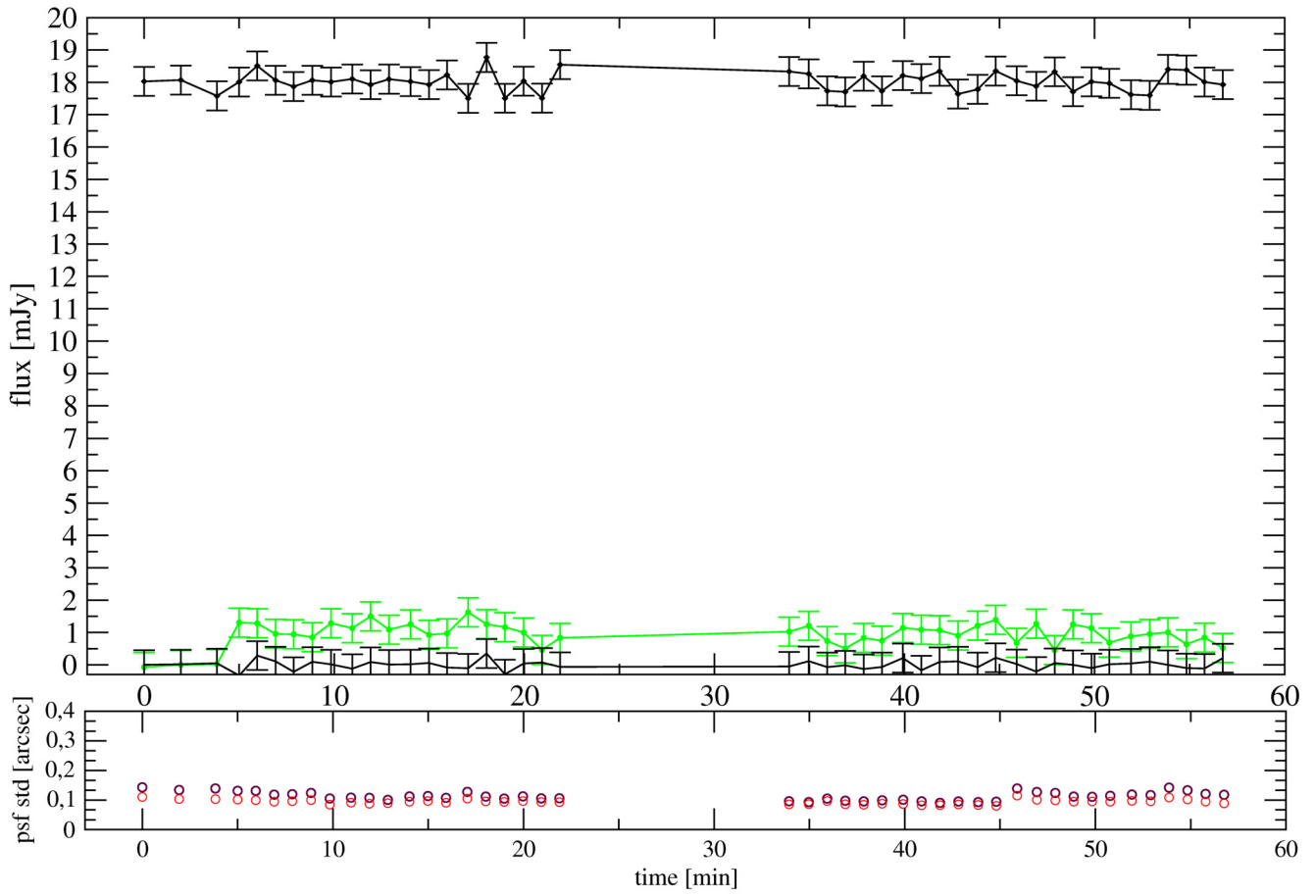


Fig. B.17. Observation from 29 April 2006.

31 May 2006

03:58:32 to 04:58:04

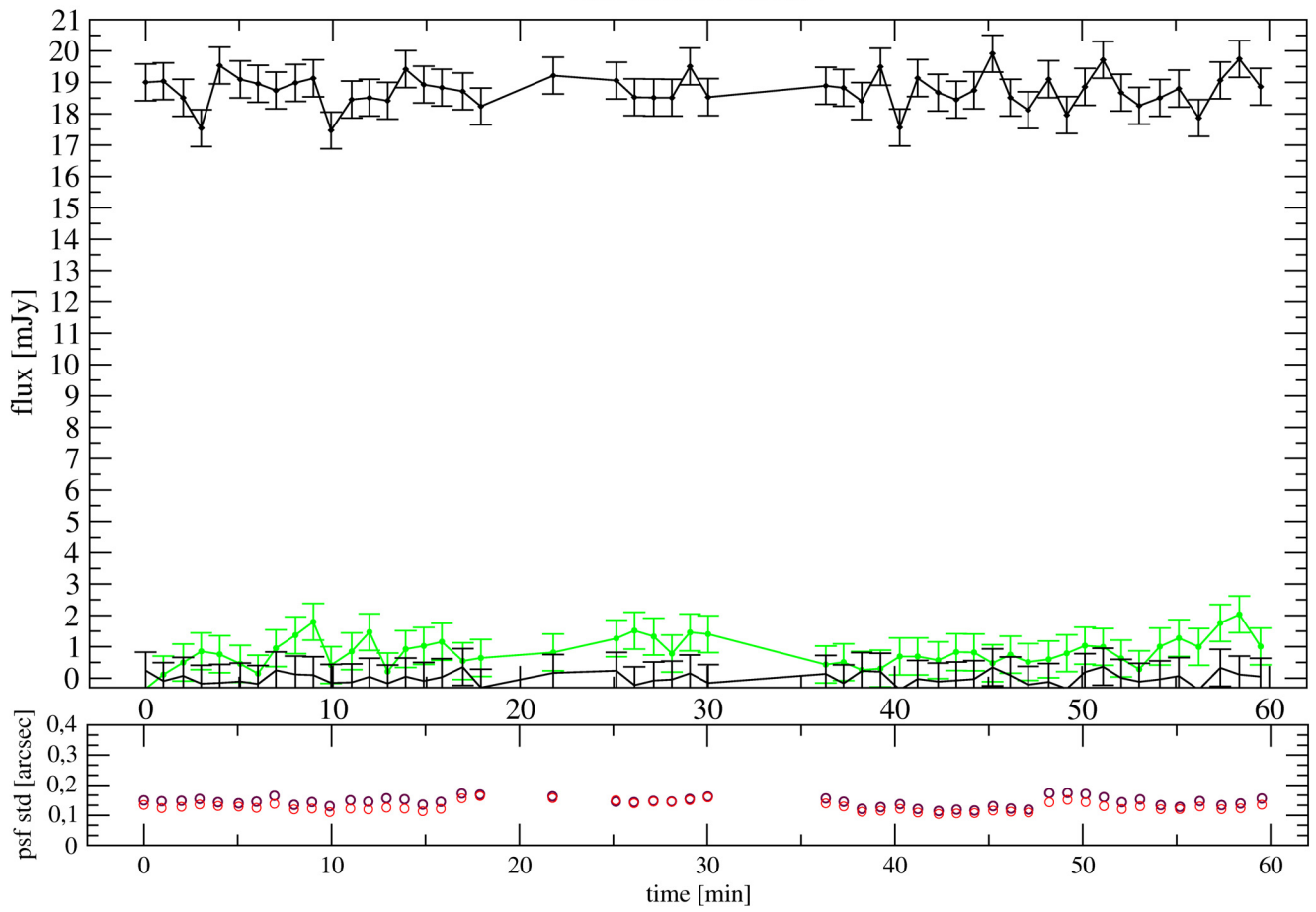
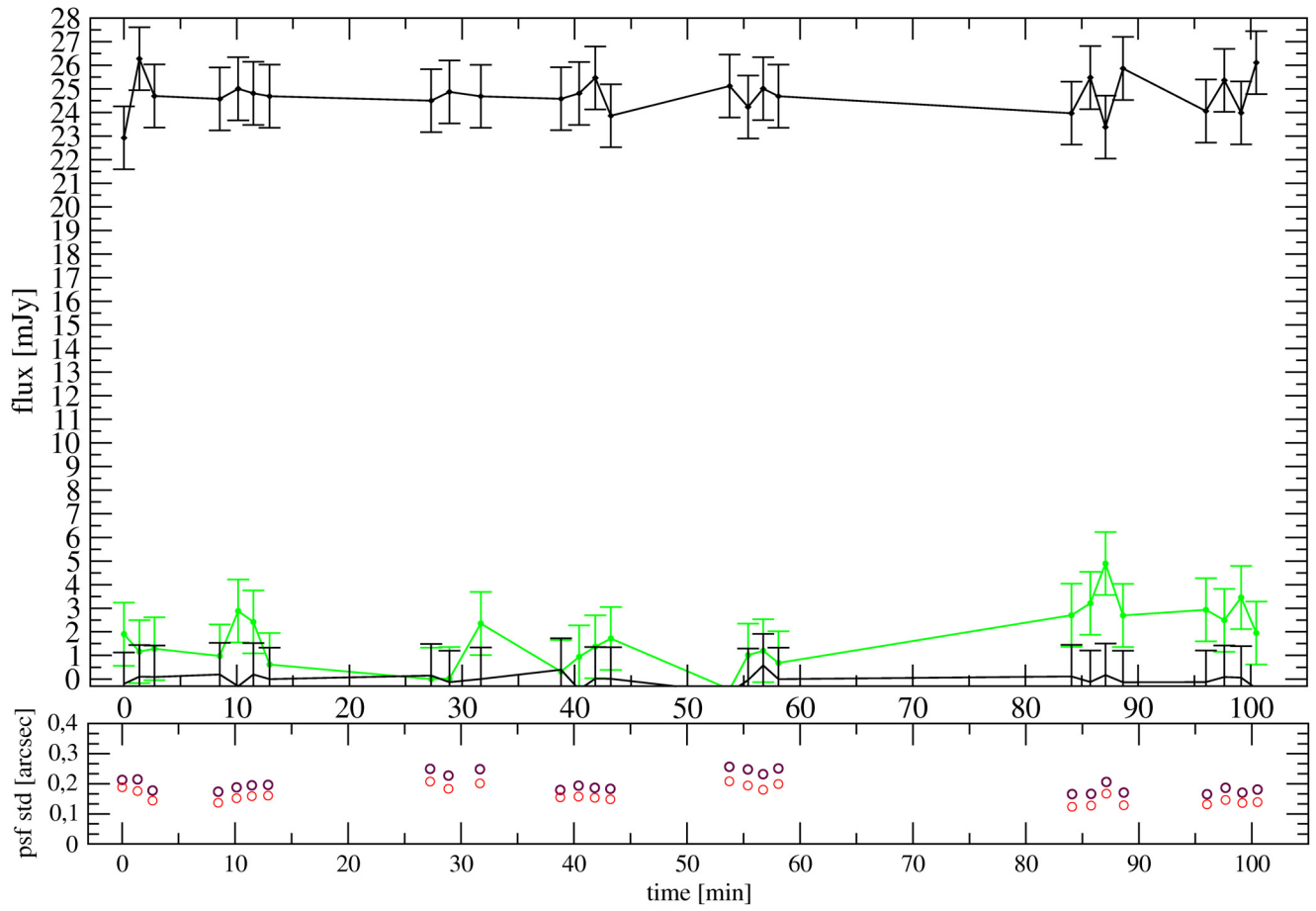


Fig. B.18. Observation from 31 May 2006.

13 June 2006

03:25:29 to 05:07:21



**Fig. B.19.** Observation from 13 June 2006. S2 is used as reference star for this lightcurve.

29 June 2006

03:56:13 to 04:48:21

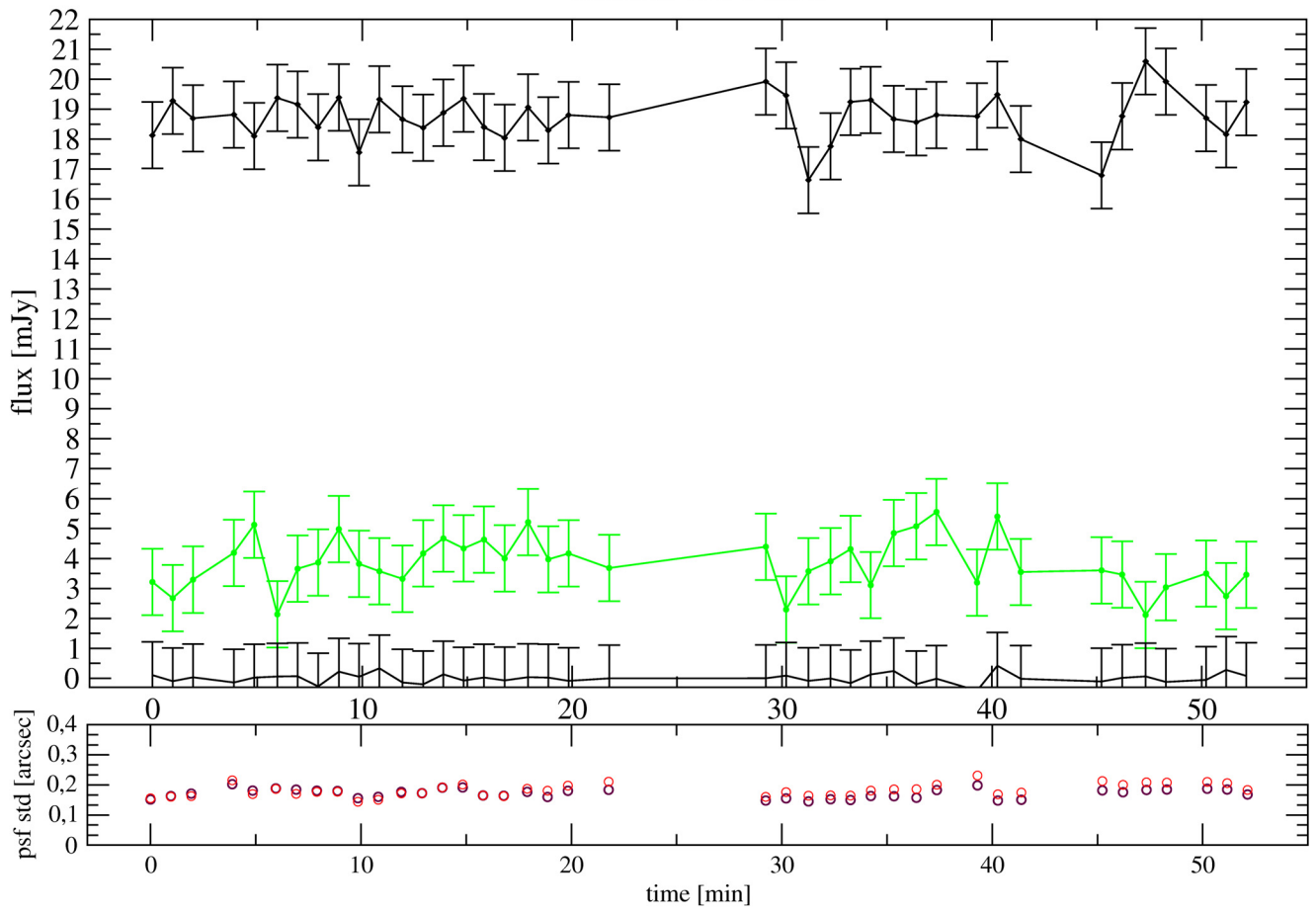
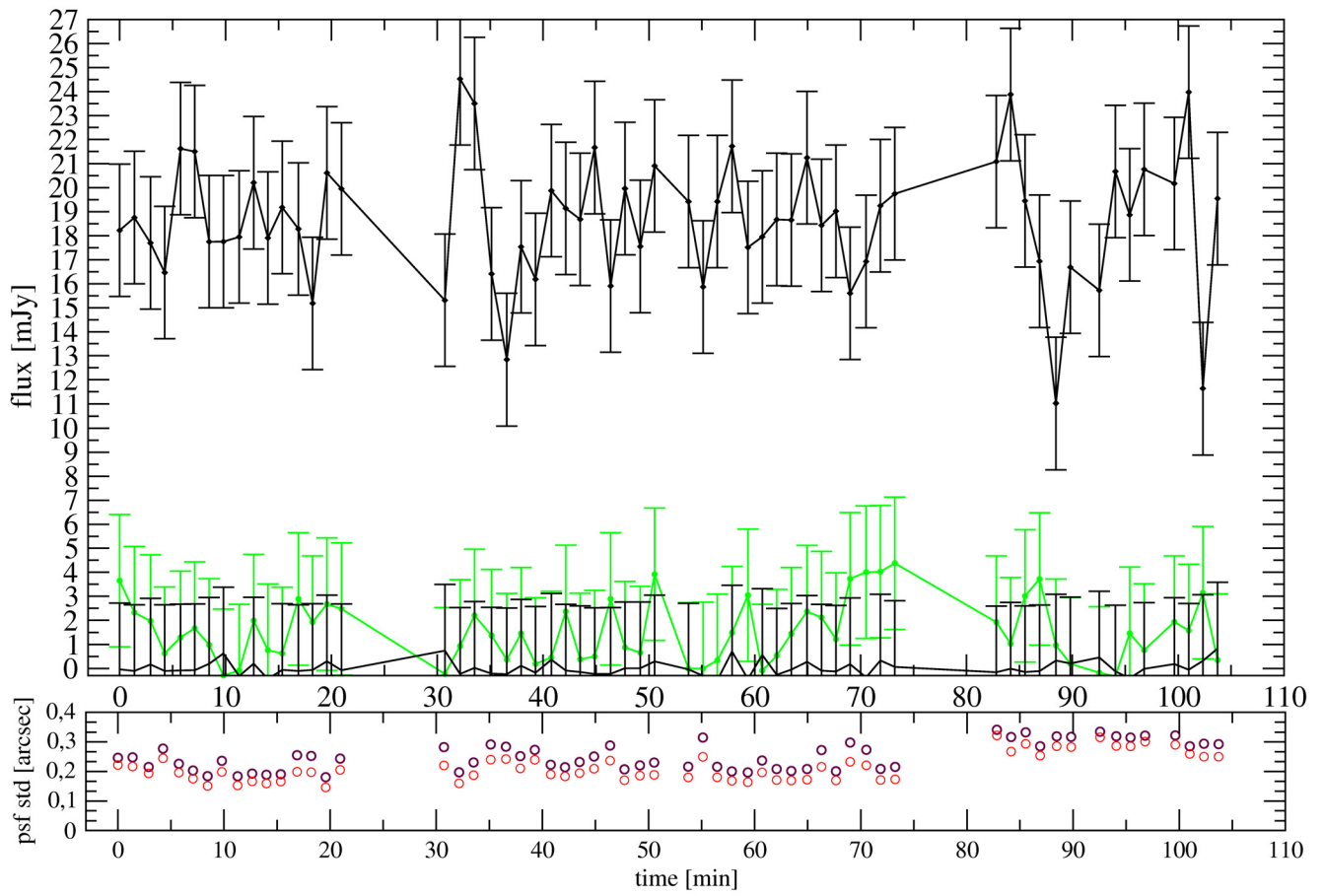


Fig. B.20. Observation from 29 June 2006.

24 July 2006

01:01:40 to 02:45:23



**Fig. B.21.** Observation from 24 July 2006.

27 July 2006

00:04:45 to 01:33:35

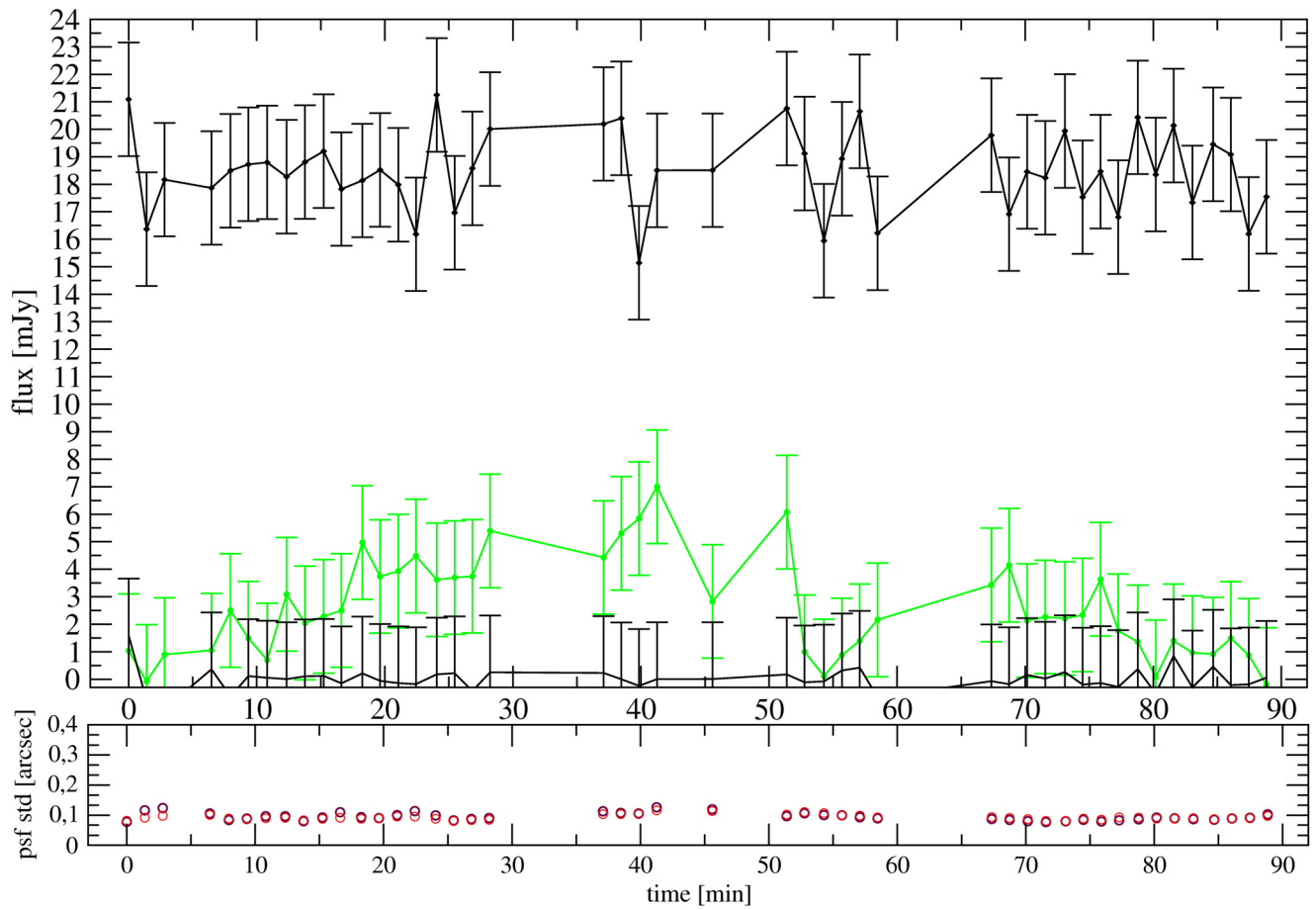


Fig. B.22. Observation from 27 July 2006.

28 August 2006

01:38:03 to 02:29:13

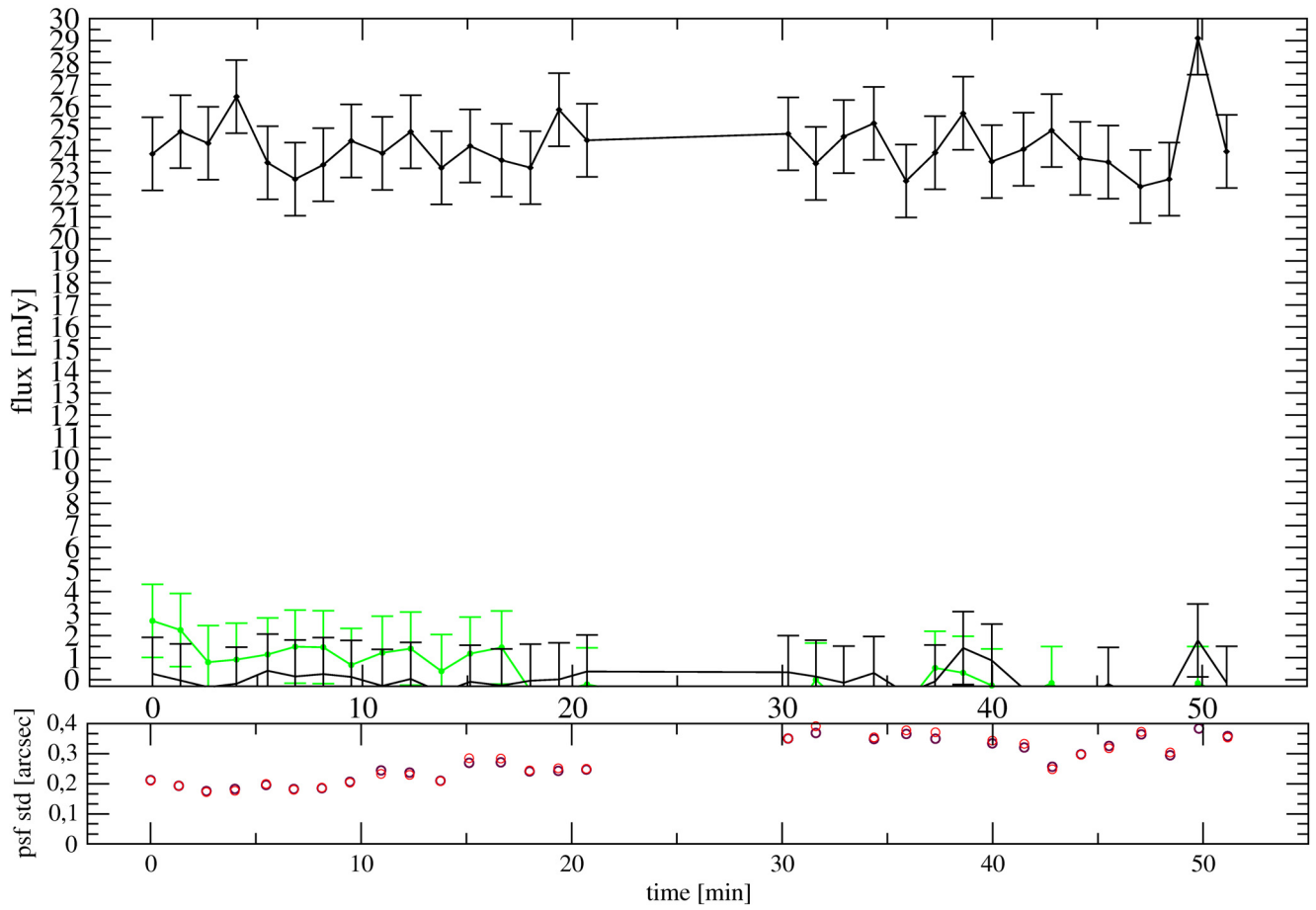
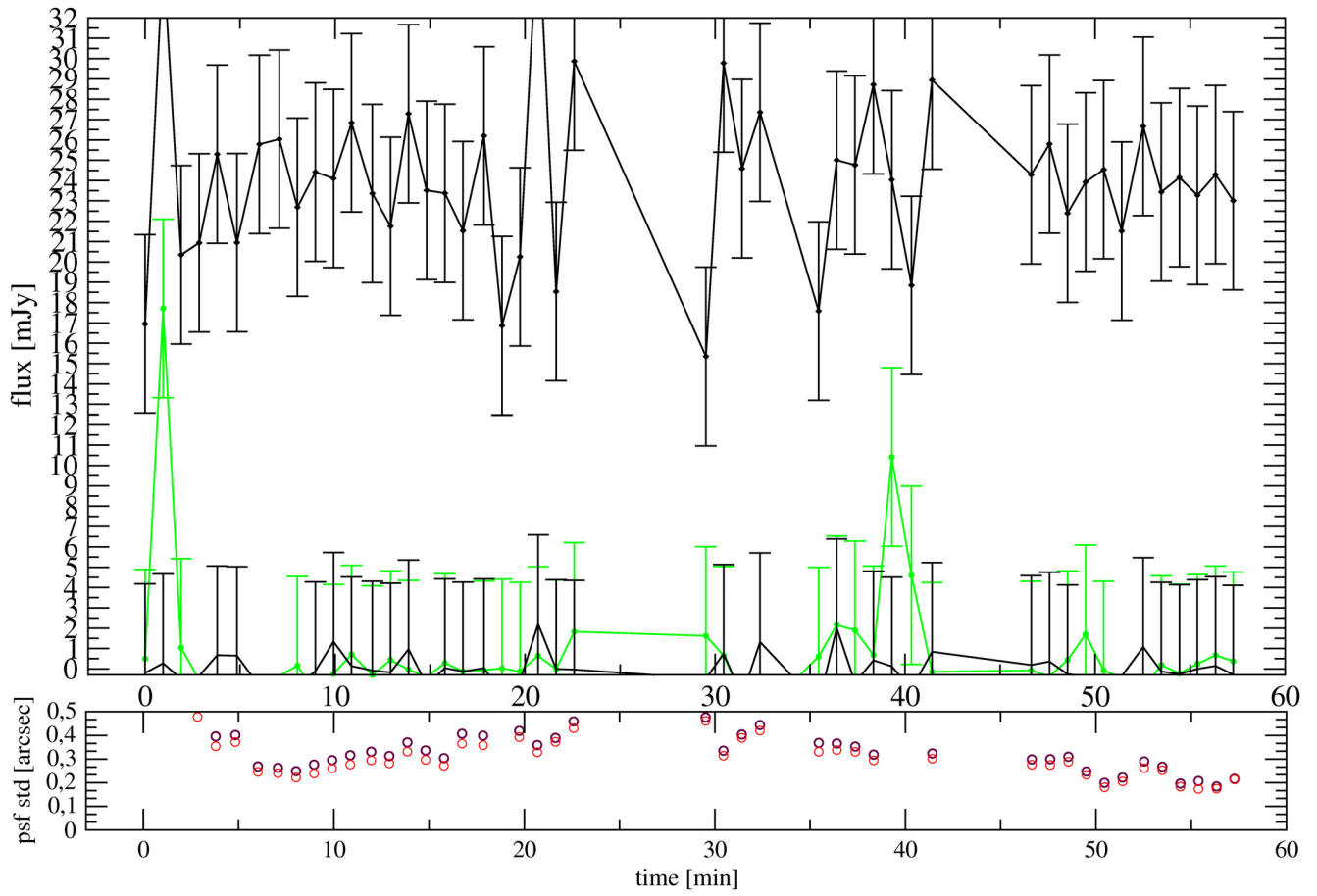


Fig. B.23. Observation from 28 August 2006.

16 September 2006

00:17:58 to 01:15:14



**Fig. B.24.** Observation from 16 September 2006.

2 October 2006

23:54:51 to 00:53:36

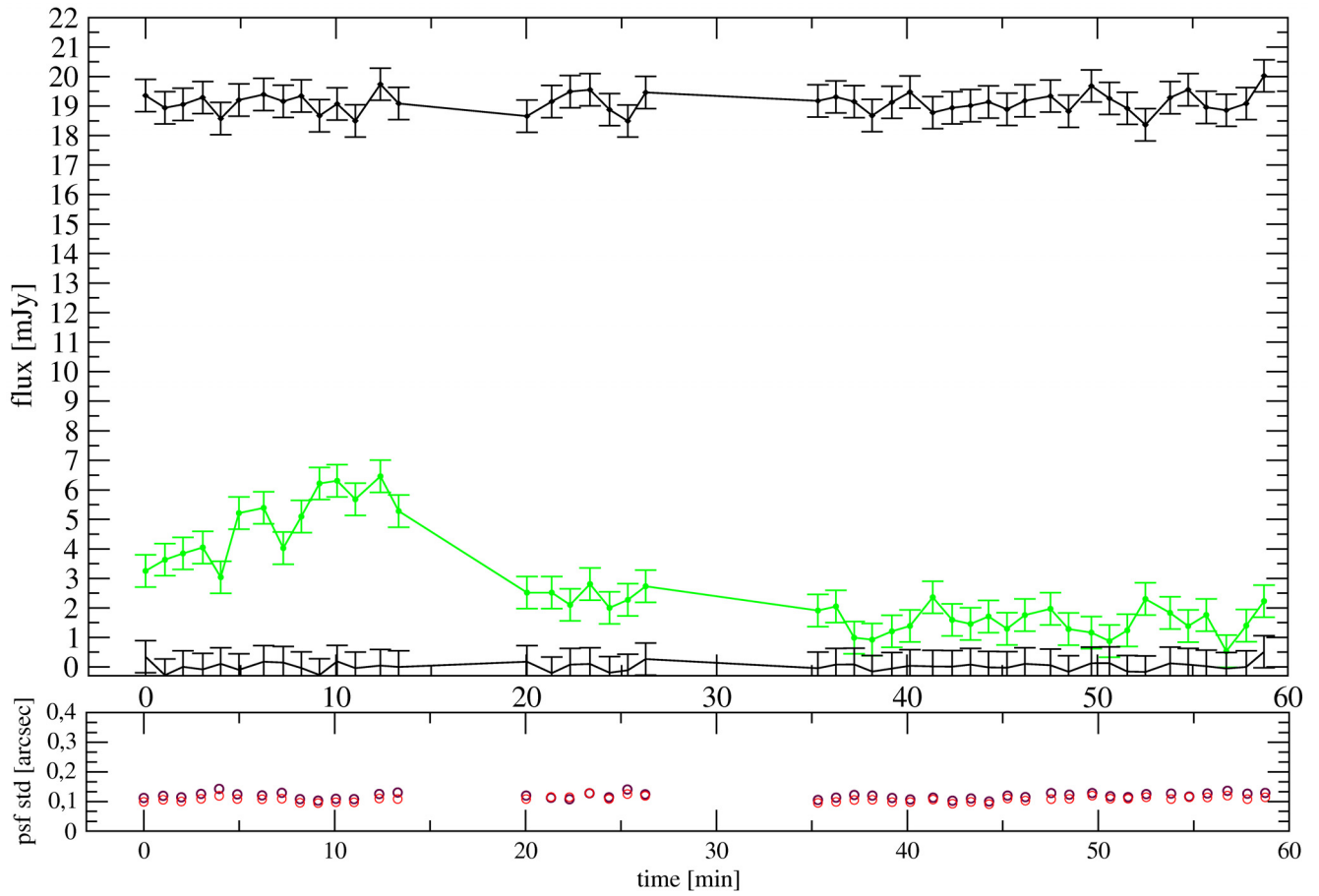


Fig. B.25. Observation from 2 October 2006.

15 October 2006

00:14:40 to 01:01:50

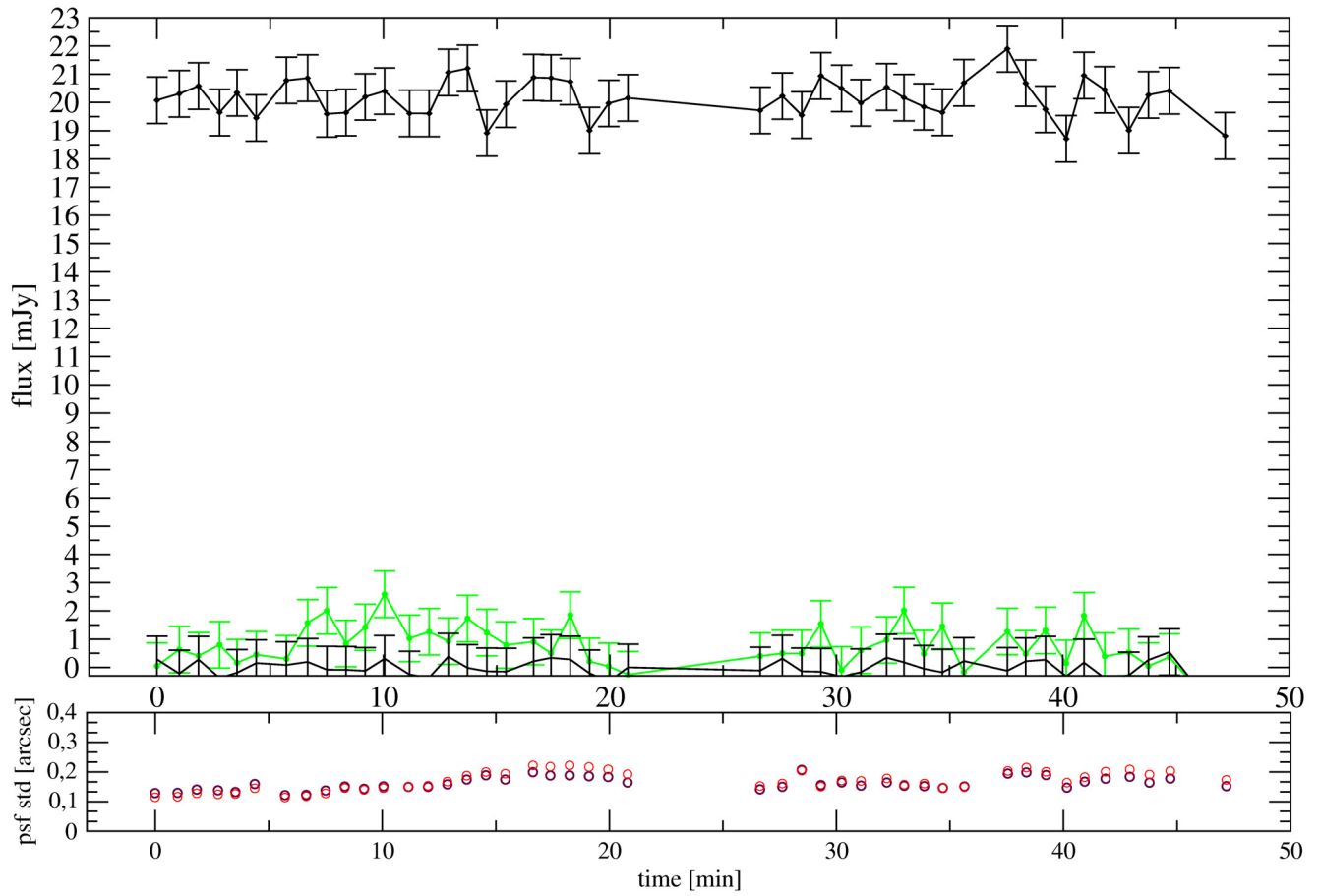


Fig. B.26. Observation from 15 October 2006.

17 March 2007

07:51:29 to 09:08:32

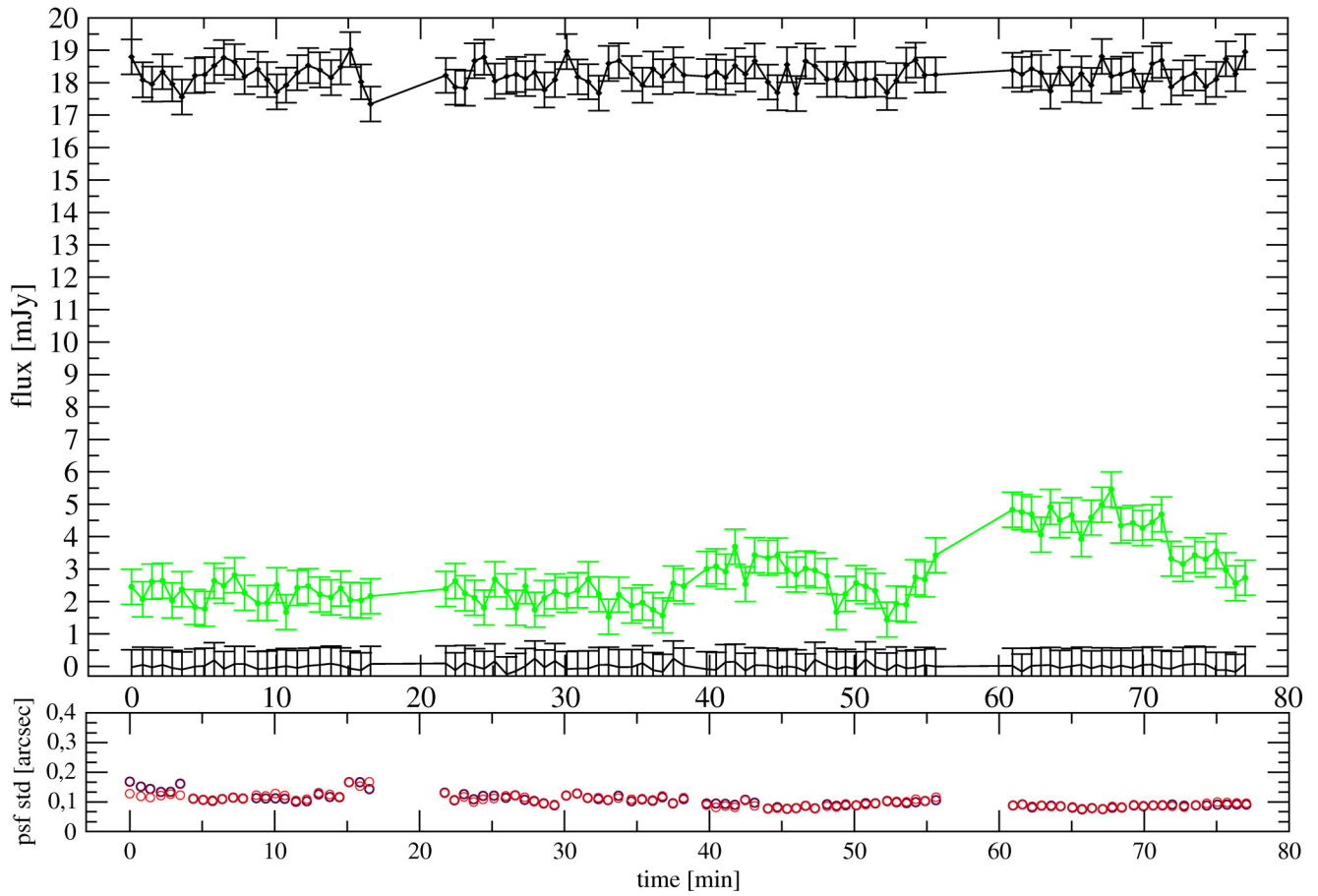


Fig. B.27. Observation from 17 March 2007.

4 April 2007

08:17:35 to 09:30:42

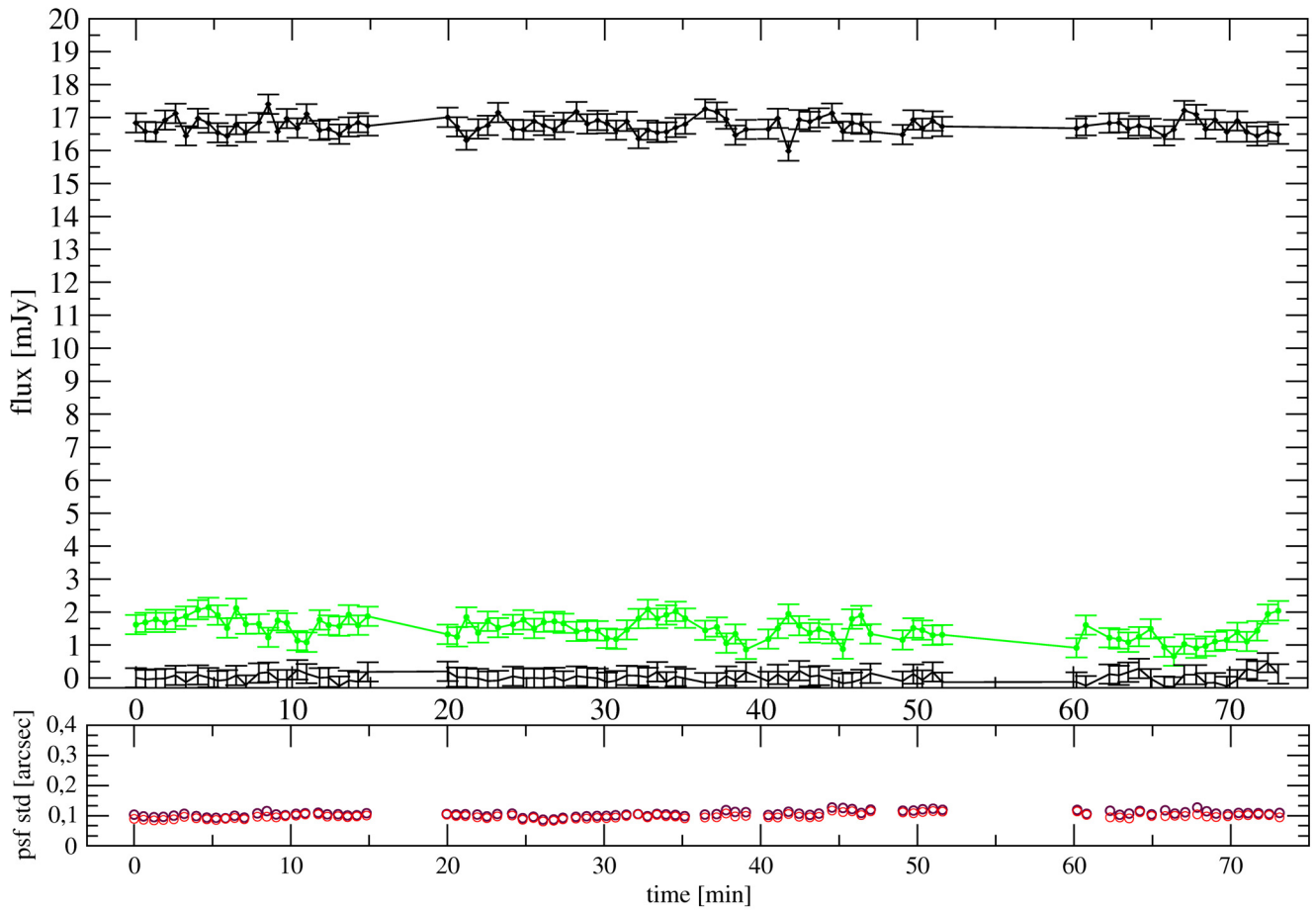


Fig. B.28. Observation from 4 April 2007.

19 July 2007

04:02:35 to 04:37:10

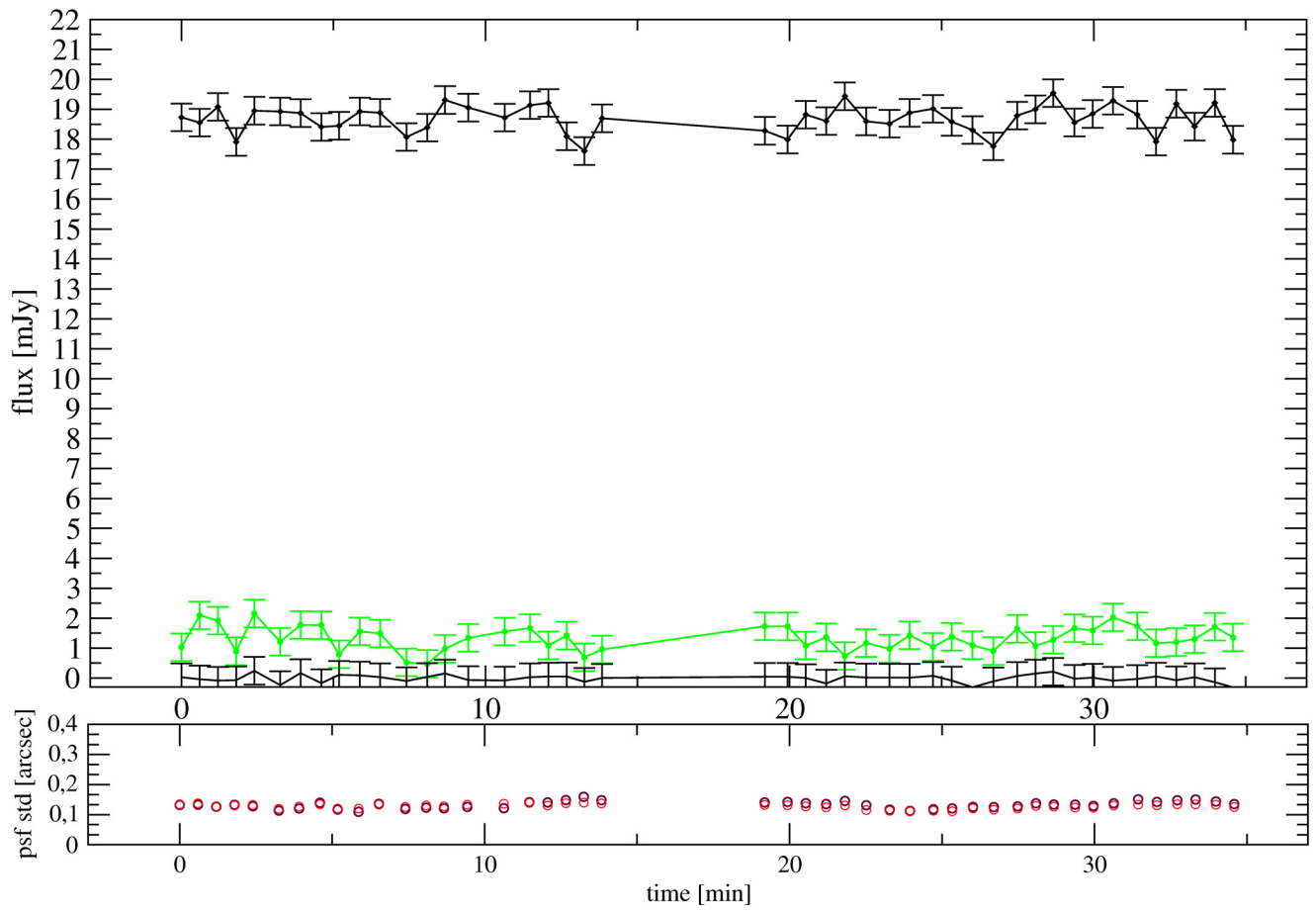
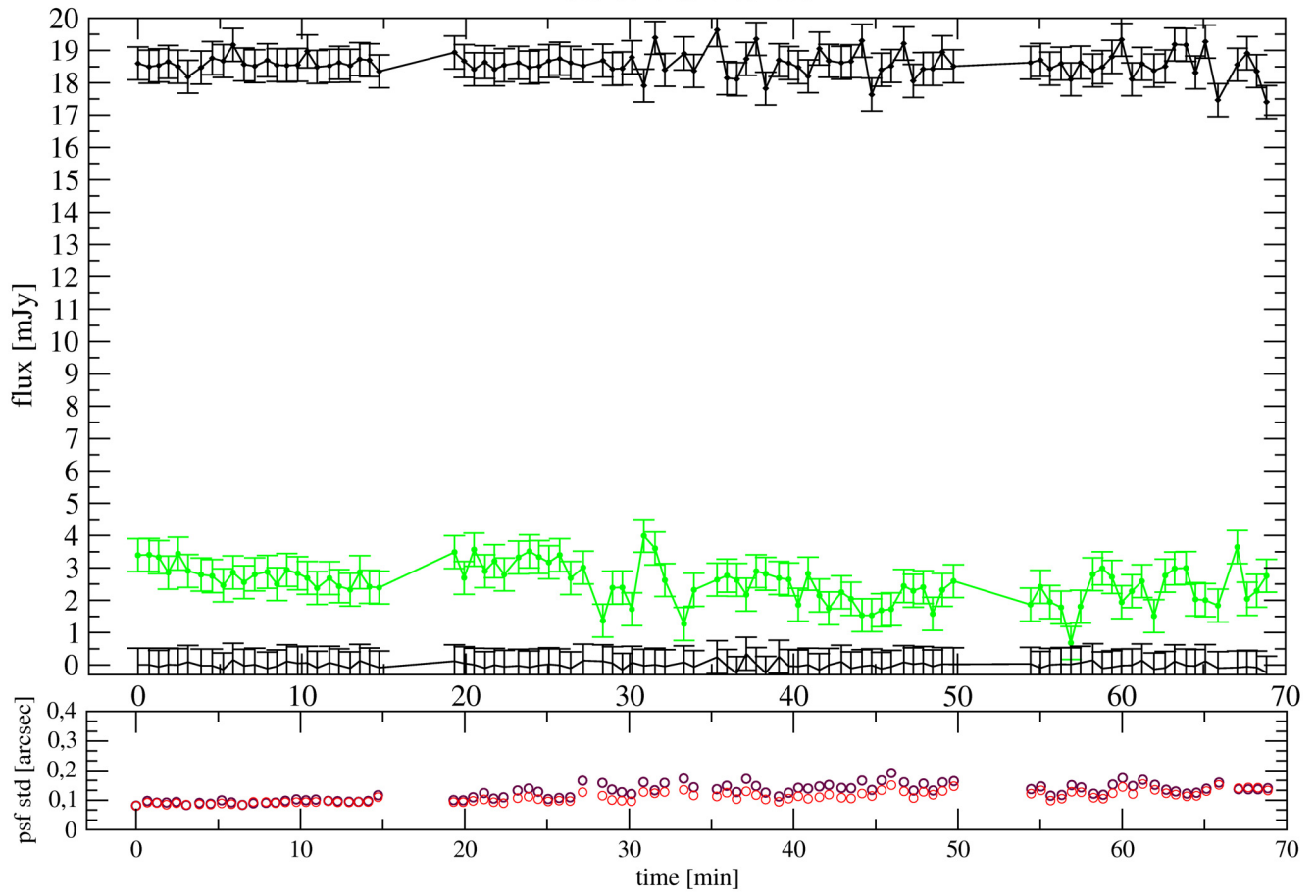


Fig. B.29. Observation from 19 July 2007.

21 July 2007

01:43:27 to 02:52:18



**Fig. B.30.** Observation from 21 July 2007.

21 June 2008

03:42:39 to 04:52:43

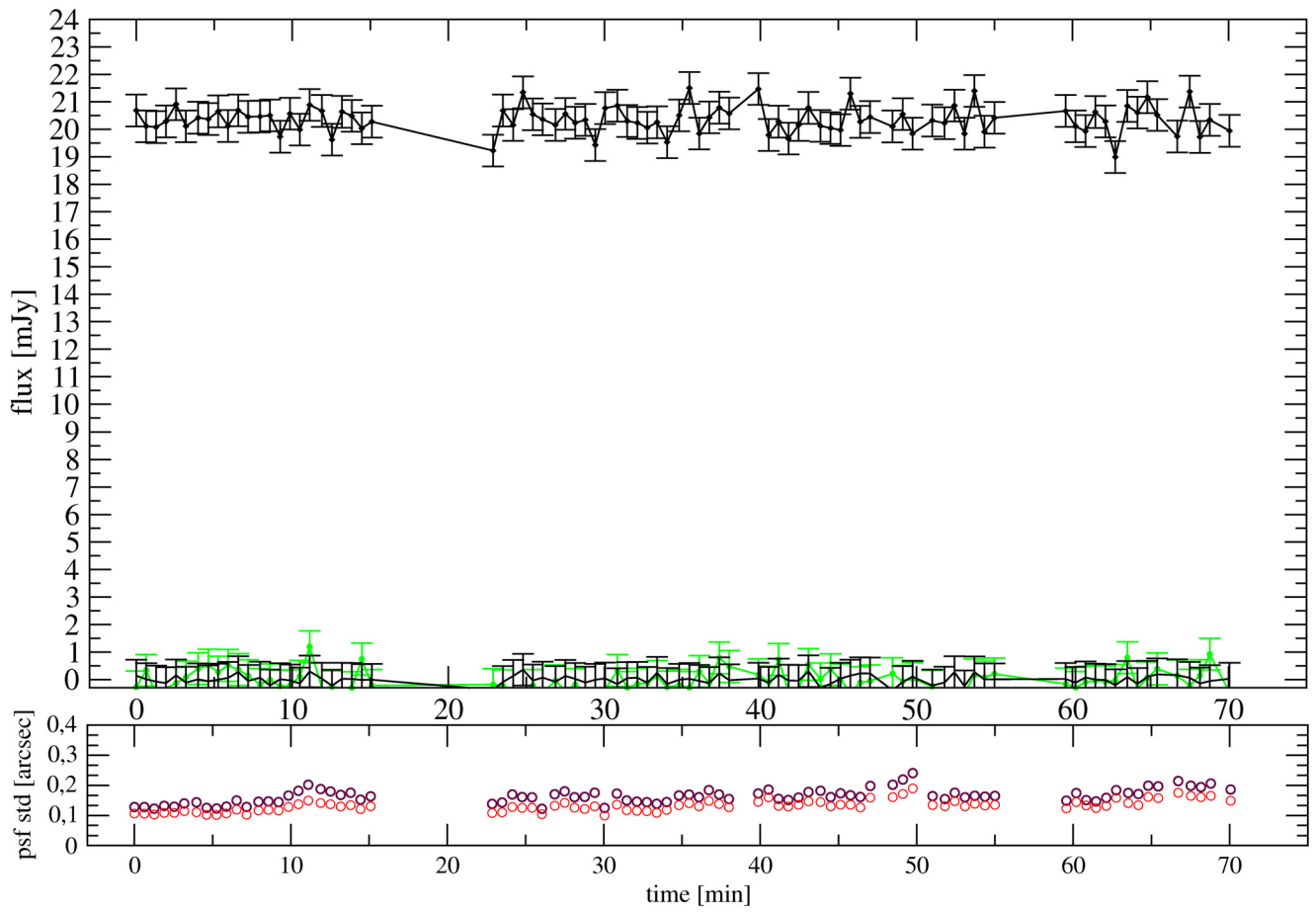


**Fig. B.31.** Observation from 21 June 2008.

22 June 2008

06:34:41 to 07:09:45

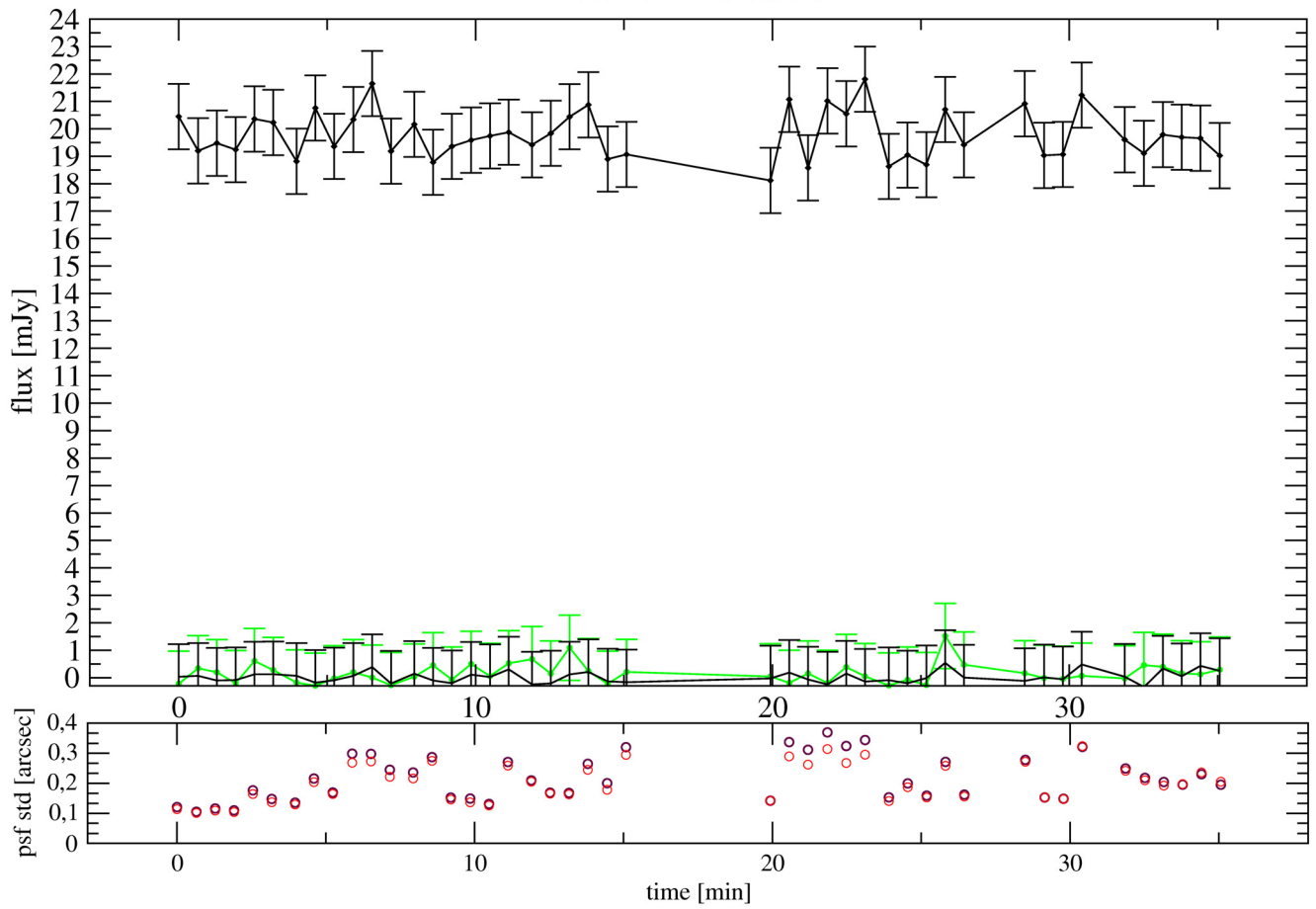


Fig. B.32. Observation from 22 June 2008.